What can we learn from REE abundances in clinopyroxene and orthopyroxene in residual mantle peridotites?

Zejia Ji[1,2], Yan Liang[1], and Boda Liu[1,*]

1 Department of Earth, Environmental and Planetary Sciences, Brown University, Providence, RI 02912, United States

2 The Key Laboratory of Orogenic Belts and Crustal Evolution, Peking University, Beijing, 100871, China

* Now at Department of Earth, Environmental and Planetary Sciences, Rice University, Houston, TX 77005, United States

Corresponding author: Yan Liang (yan_liang@brown.edu)

Abstract

Clinopyroxene and orthopyroxene are the two major repositories of rare earth elements (REE) in spinel peridotites. Most geochemical studies of REE in mantle samples focus on clinopyroxene. Recent advances in in situ trace element analysis has made it possible to accurately measure REE abundance in orthopyroxene. The purpose of this study is to determine what additional information one can learn about mantle processes from REE abundances in orthopyroxene coexisting with clinopyroxene in residual spinel peridotites. To address this question, we select a group of spinel peridotite xenoliths (9 samples) and a group of abyssal peridotites (12 samples) that are considered residues of mantle melting and that have mineral modes and major element and REE abundances reported in the two pyroxenes in the literature. We use a multi-mineral disequilibrium melting model and the Markov chain Monte Carlo method to invert melting parameters from REE abundance in the bulk sample. We then use a subsolidus reequilibration model to calculate REE redistribution between cpx and opx at the extent of melting inferred from the bulk REE data and at the closure temperature of REE in the two pyroxenes. We compare the calculated results with those observed in clinopyroxene and orthopyroxene in the

mantle sample. Results from our two-step modeling show that it is more reliable to deduce melting parameters from REE abundance in the bulk peridotite than in clinopyroxene. We do not recommend the use of REE in clinopyroxene alone to infer the degree of melting experienced by the mantle xenolith, as HREE in clinopyroxene in the xenolith are reset by subsolidus reequilibration. In general, LREE in orthopyroxene and HREE in clinopyroxene are more susceptible to subsolidus redistribution. The extent of redistribution depends on the modes of clinopyroxene and orthopyroxene in the sample and thermal history experienced by the peridotite. By modeling subsolidus redistribution of REE between orthopyroxene and clinopyroxene after melting, we show that it is possible to discriminate mineral mode of the starting mantle and cooling rate experienced by the peridotitic sample. We conclude that endmembers of the depleted MORB mantle and the primitive mantle are not homogeneous in mineral mode. A modally heterogeneous peridotitic starting mantle provides a simple explanation for the large variations of mineral mode observed in mantle xenoliths and abyssal peridotites. Finally, by using different starting mantle compositions in our simulations, we show that composition of the primitive mantle is more suitable for modeling REE depletion in mantle xenoliths than the composition of the depleted MORB mantle.

1. INTRODUCTION

Abundances of rare earth element (REE) in mantle rocks have been widely used to study partial melting, melt migration and melt-rock interaction processes in the mantle. Most geochemical studies of REE in spinel peridotites focus on clinopyroxene (cpx) which is the major repository of REE in the peridotites. Important conclusions based on REE abundances in cpx in abyssal peridotites include (1) samples with depleted LREE are resulted from fractional or near fractional melting (Johnson et al., 1990; Johnson and Dick, 1992; Kelemen et al., 1997; Niu and Hékinian, 1997; Shimizu, 1998; Hellebrand et al., 2001; Brunelli et al., 2006; Liang and Peng, 2010); (2) samples with elevated LREE are due to melt impregnation and melt-rock interaction (Hellebrand et al., 2002; Warren et al., 2009; Brunelli et al., 2014); and (3) cpx with higher HREE but depleted LREE is attributed to melting starting in the garnet stability field in the upwelling mantle (Johnson et al., 1990; Hellebrand et al., 2002; Brunelli et al., 2006). However, not all of the interpretations are unique. For examples, the slightly elevated LREE patterns in abyssal

peridotites that show no obvious signs of melt addition can also be explained by small extent of disequilibrium melting (Liang and Liu, 2016; Liu and Liang, 2017). Near fractional melting starting in the garnet stability field failed to explain some samples with elevated HREE patterns (Liang and Peng, 2010). One possible explanation of the higher than expected HREE in residual cpx is subsolidus redistribution (Sun and Liang, 2014). During subsolidus reequilibration, REE is strongly and preferentially partitioning into cpx relative to orthopyroxene (opx) and olivine in spinel peridotites (e.g., Stosch, 1982; Witt-Eickschen and O'Neill, 2005; Lee et al., 2007; Liang et al., 2013; Sun and Liang, 2014). To sort out the various magmatic and subsolidus processes affecting the abundance and distribution of REE and other trace elements in residual peridotites, additional information is needed.

Recent advances in in situ trace element analysis makes it possible to measure REE and other incompatible trace elements in opx. An increasing number of geochemical studies of spinel peridotites have reported REE in both cpx and opx (e.g. Hellebrand et al., 2005; Warren et al., 2009; Brunelli and Seyler, 2010; Seyler et al., 2011; D'Errico et al., 2016). These additional data not only can be used to reconstruct bulk trace element compositions for samples that experienced secondary alteration, but also offer an opportunity for a more complete assessment of the thermal and magmatic history experienced by the peridotite. To learn more from REE abundances in coexisting cpx and opx in residual peridotite samples, we use a multi-mineral disequilibrium melting model and a subsolidus reequilibration model to investigate how REE in the bulk residue are fractionated during decompression melting along a mantle adiabat and how REE in residual cpx and opx are redistributed during subsolidus reequilibration. In a close system, REE abundance in the bulk sample is independent of subsolidus reequilibration, whereas REE abundances in coexisting cpx and opx are sensitive to temperature and mineral mode. Hence it is more advantageous to infer melting parameters from REE abundance in the bulk sample than in cpx alone. As will be demonstrated in this study, it is possible to constrain mineral mode in the starting mantle and thermal history of the residual peridotites based on REE abundances in cpx and opx.

The remaining of this paper is organized as follows. In Section 2, we briefly describe key parameters used in the disequilibrium melting model detailed in Appendix A and the procedure used in the subsolidus reequilibration calculation. In Section 3, we present two case studies of REE abundance and distribution in selected residual spinel peridotites from cratons (mantle xenoliths)

and mid-ocean ridges (abyssal peridotites). In Section 4, we discuss additional processes or factors that may contribute to the variations of REE in the bulk and two pyroxenes in some of the samples included in this study. We then compare melting parameters derived from REE in the bulk and cpx alone for the selected mantle xenoliths and abyssal peridotite samples. Finally, in Section 5, we summarize the main results of this study. The methodology developed in this study is general and can be used to study the abundance and distribution of REE as well as other incompatible trace elements in residual mantle samples from a variety of tectonic settings.

2. MELTING FOLLOWED BY SUBSOLIDUS REEQUILIBRATION

2.1. Model description

We are interested in the fractionation of REE in cpx and opx during decompression melting in an upwelling steady-state mantle column and the redistribution of REE between cpx and opx at a subsolidus temperature after melting. We use the multi-mineral disequilibrium melting model of Liang and Liu (2016) to simulate REE depletion during partial melting along a mantle adiabat. Key features of the melting model include channelized melt extraction and diffusion-limited chemical exchange between the pyroxenes and the interstitial melt. Because diffusivities of REE in olivine and garnet are considerably larger than those in the pyroxenes (Van Orman et al., 2001, 2002; Cherniak and Liang, 2007; Cherniak, 2015) and abundances of REE in olivine and spinel are much smaller than those in the pyroxenes, it is reasonable to assume that olivine and spinel (also garnet for melting in the garnet stability field) are in local chemical equilibrium with their interstitial melt during melting.

The governing mass conservation equations and their simplifications are summarized in Appendix A. There are four dimensionless parameters in the multi-mineral disequilibrium melting model for this problem: degree of melting experienced by the residual mantle (F), fraction of melt extracted to the channel ($\mathbb{R}$, called melt suction rate hereafter), disequilibrium parameter of La in cpx (ε_{cpx}^{La}), and relative diffusion rate of REE in cpx and opx ($\frac{R_{cpx}}{R_{opx}}$). The limits of perfect fractional melting and batch melting are realized when $\mathbb{R} = 0$ and $\mathbb{R} = 1$, respectively. The limit of equilibrium melting is realized when $\varepsilon_{cpx}^{La} = 0$. The diffusive exchange rate constants for an REE

in opx (R_{opx}) and cpx (R_{cpx}) are inversely proportional to the diffusive time scales for opx and cpx (Navon and Stolper, 1987; Bodinier et al., 1990; Liang, 2003):

$$R_{opx} = \frac{3\beta D_{opx}}{d_{opx}^2} \ , \ R_{cpx} = \frac{3\beta D_{cpx}}{d_{cpx}^2} \ , \qquad (1a, 1b)$$

where D is the diffusion coefficient of REE in opx or cpx; d is the average or effective mineral grain size of opx or cpx; and β is a geometric factor. The relative diffusion rate for an REE is given by the expression:

$$\frac{R_{opx}^{REE}}{R_{cpx}^{REE}} = \frac{D_{opx}^{REE}}{D_{cpx}^{REE}} \frac{d_{cpx}^2}{d_{opx}^2} . \qquad (2)$$

The disequilibrium parameter is a measure of bulk melting rate relative to diffusion rate for the element of interest in a mineral (Eq. A1d in Appendix A). Given the disequilibrium parameter of La in cpx, disequilibrium parameters for other REE in cpx can be calculated according to their diffusivity ratio (Liang and Liu, 2016):

$$\varepsilon_{cpx}^{REE} = \frac{D_{cpx}^{La}}{D_{cpx}^{REE}} \varepsilon_{cpx}^{La} . \qquad (3)$$

During decompression melting along a mantle adiabat, temperature decreases upward in the melting column. In this study, we calculate the relative diffusion rate and disequilibrium parameters using experimentally determined diffusion parameters for REE in cpx and opx (Van Orman et al., 2001, 2002; Cherniak and Liang, 2007). For convenience of numerical calculations, we scale the disequilibrium parameters in Eq. 3 by their respective values at 1300°C,

$$\varepsilon_{cpx}^{T} = \frac{D_{cpx}^{1300}}{D_{cpx}^{T}} \varepsilon_{cpx}^{1300} \ . \qquad (4)$$

In the simulations presented below, we treat ε_{cpx}^{1300} for La in cpx as a free parameter and calculate the disequilibrium parameter at other temperatures using Eq. 4. Variations of the disequilibrium parameter of La in cpx as a function of temperature and degree of melting along a 1300 °C mantle adiabat can be found in supplementary Fig. S1.

We use the temperature and major element composition dependent opx-cpx and olivine-cpx REE partitioning models of Sun and Liang (2014) and mineral mode in the sample to calculate REE abundances in coexisting opx and cpx at a subsolidus temperature after melting. In a closed system, concentration of a trace element in the bulk peridotite (C_s) depends on mineral mode and mineral composition, but is independent of temperature, viz.,

$$C_s = w_{cpx}C_{cpx} + w_{opx}C_{opx} + w_{ol}C_{ol} + w_{sp}C_{sp}\,, \tag{5}$$

where w_j and C_j are the weight fraction of and trace element concentration in mineral j in the residual peridotite, respectively. Since REE abundances in olivine and spinel are much lower than those in cpx and opx, concentrations of a REE in cpx and opx at a given temperature (T) can be calculated using the expressions (see also Eq. A2e in Appendix A):

$$C_{cpx}\,(T) = \frac{C_s}{w_{cpx}+w_{opx}\,k_{opx-cpx}}\,, \tag{6a}$$

$$C_{opx}(T) = k_{opx-cpx}C_{cpx}\,, \tag{6b}$$

where $k_{opx\text{-}cpx}$ is the temperature and major element composition dependent opx-cpx REE partition coefficient. In the case studies presented in Section 3, we set the temperature in Eqs. 6a and 6b to the closure temperature of REE based on the REE-in-two-pyroxene thermometer of Liang et al. (2013).

2.2. Forward simulations of REE in pyroxenes during melting and subsolidus reequilibration

Variations of REE in opx and cpx in residual peridotites that have experienced decompression melting and subsolidus reequilibration can be visualized through forward simulations using the two-step melting followed by subsolidus reequilibration model outlined in Section 2.1. Figure 1a shows one such example for a case of 6% near fractional melting ($\mathbb{R}$ = 0.95, ε_{La}^{1300} = 0.01) of spinel lherzolite along the 1300 °C adiabat. Melting strongly depletes LREE in both cpx and opx, hence the bulk rock (solid lines in Fig. 1a). Since REE abundances in cpx are considerably higher than those in opx, olivine and spinel, REE pattern of the bulk residue follows that of cpx, forming subparallel trends in the chondrite-normalized REE diagram (Fig. 1a). To the first order, REE abundance in the bulk rock is proportional to the amount of cpx in the residue, viz., $C_s \sim w_{cpx}{*}C_{cpx}$. This is demonstrated in Fig. 1a where the abundance of REE in cpx is about

7 times that in the bulk rock and the modal abundance of cpx in the residue after 6% of melt is 13.6 %. The close similarity between REE in the bulk rock and its constituent cpx forms the basis for using REE in cpx to study mantle melting processes in the literature.

Figure 1a also shows that REE pattern of residual opx differs considerable from those of cpx and the residue: light and middle REE are preferentially depleted in opx relative to those in the bulk or cpx whereas heavy REE in opx are comparable to those in the bulk rock. This is due to the smaller M2 site of opx structure, making LREE more incompatible in opx than in cpx. The net effect is a steeper LREE depleted pattern for opx in the REE diagram. The REE pattern in opx can be further complicated by subsolidus reequilibration: with decreasing temperature, LREE is preferentially redistributed from opx to cpx, shifting the entire opx REE pattern below that produced by partial melting (cf. dashed and solid green lines in Fig. 1a). Although it is not straightforward to infer mantle melting processes based on REE abundances and patterns in opx in residual peridotites, abundances of REE in opx may offer useful information on the thermal history experienced by the peridotite (e.g., Liang et al., 2013; Dygert and Liang, 2015; Wang et al., 2015; Dygert et al., 2017) and mineral modes in the starting mantle. We will demonstrate these points in Sections 3 and 4. However, due to the ionic size-dependent REE partitioning between opx and cpx, subsolidus reequilibration mildly elevates HREE in cpx (Fig. 1a), which may complicate the interpretation of garnet signal in residual spinel lherzolite and harzburgite (Sun and Liang, 2014). Since the abundance of LREE is considerably lower in residual opx, LREE in cpx are not sensitive to subsolidus redistribution in spinel lherzolite. When the degree of melting is large, the modal abundance of cpx decreases in the residue, and the effect of subsolidius reequilibration on the LREE in cpx will be more significant. Supplementary Fig. S2 presents a calculated example for a case of 15% near fractional melting ($\mathbb{R}$ = 0.95, ε_{La}^{1300} = 0.01).

The mineral grain size also affects REE abundances in cpx and opx during disequilibrium melting and subsequent cooling through the relative diffusive exchange rate (Eq. 2). In general, grain size of opx (2-5 mm) is larger than grain size of cpx (1-2 mm) in residual spinel peridotites. The effect of chemical disequilibrium increases with increasing opx grain size, leading to an increase in the effective partition coefficient for REE between opx and its coexisting melt (Liang and Liu, 2016). This can be demonstrated through a forward simulation in which we increase the relative opx-to-cpx grain size from 1 to 5 while keeping the cpx grain size to 1 mm. As shown in

Fig. 1b, the calculated middle and heavy REE abundances in cpx slightly decrease whereas the light REE abundances in opx significantly increase compared to the case of 1 mm opx. Consequently, the simulated bulk REE is not very sensitive to the choice of opx/cpx grain size ratio. Regardless how REE are distributed between opx and cpx, the REE abundance in the bulk residue remains the same as that produced by partial melting. Hence it is more reliable to use REE in the bulk rock to infer melting processes experienced by residual peridotites than REE in cpx alone. We will demonstrate this point through two case studies below.

3. READING MAGMATIC AND THERMAL HISTORY FROM REE ABUNDANCES IN BULK PERIDOTITES AND TWO PYROXENES: AN INVERSE STUDY

The multi-mineral disequilibrium melting model can be used to infer melting parameters from measured REE abundance in bulk residual peridotites through inverse geochemical modeling. In this study we investigate REE + Y abundances in selected spinel peridotite samples from cratons (mantle xenoliths) and mid-ocean ridges (abyssal peridotites). We include Y in our analysis because it behaves similarly to HREE during mantle melting and its abundance is routinely measured along with REE in opx and cpx. Peridotites from stable cratons are generally well-equilibrated and have similar and relatively low equilibrium or closure temperatures for both major elements and REE in coexisting cpx and opx, whereas abyssal peridotites have higher closure temperatures for REE than major elements in pyroxenes (Liang et al., 2013; Dygert and Liang, 2015; Wang et al., 2015). This is illustrated in Fig. 2 for the selected samples in this study. Since abyssal peridotites are variously serpentinized and some mantle xenoliths contain glass veins, we use measured REE + Y abundances in minerals (cpx, opx, and olivine when available) and mineral modes reported in the literature to reconstruct bulk REE + Y abundances in the peridotites. As shown in Fig. 1, the light and middle REE in opx are considerably lower than those in cpx, making accurate measurements of these elements in opx an analytical challenge. This problem is especially prevalent for odd atomic number elements such as La (57) and Pr (59), resulting in scattered LREE patterns in some samples. To include more elements and more samples in this study, we applied an interpolation procedure to some of the samples that exhibit scattered REE patterns. The procedure, detailed in Supplementary Materials, is based on correlation between the nearest neighbor REE (e.g., La and Ce) established by mantle pyroxenes that have smooth REE patterns.

In Supplementary Table S1a, we list mineral modes and REE abundances in cpx, opx, and the bulk peridotite included in this study.

In order to use the multi-mineral disequilibrium melting model to calculate the melting parameters from the bulk REE + Y abundance in residual peridotites, we need to know mineral grain size, mineral mode, and composition of the starting mantle. Following standard practice in REE modeling, we assume that abundances of REE + Y in the starting mantle are the same as the average DMM (Workman and Hart, 2005) for abyssal peridotites and the primitive mantle (PM, McDonough and Sun, 1995) for mantle xenoliths. We will discuss effects of other starting mantle compositions in Section 4. The mineralogy of the starting mantle is a primitive spinel lherzolite. (Effect of garnet field melting will be discussed in Section 3.2.) There are some uncertainties in the mineral mode of the starting mantle. For example, the DMM of Workman and Hart (2005) consists of 13% cpx, 28% opx, 57% olivine, and 2% spinel, whereas the starting mantle of Johnson (1998) and Hellebrand et al. (2002) has 17% cpx, 27% opx, 53% olivine, and 3% spinel. The latter has been used in our recent studies of REE depletion in residual cpx from abyssal peridotites (Liang and Peng, 2010; Liang and Liu, 2016; Liu and Liang, 2017). Figs. 3a and 3b show large variations in mineral modes in both mantle xenoliths and abyssal peridotites (see also Fig. 4 in Warren, 2016 for more abyssal peridotite data). Even for the small number of samples included in the present study, the range of modal variations cannot be explained by a single melting trend or melting reaction using either of the starting mode mentioned above. It is possible that mineral modes are not well constrained for some of the peridotite samples (e.g., heavily serpentinized abyssal peridotites). Estimates of modal abundance of fresh mantle xenoliths are typically made through mass balance calculations using measured major and minor element concentrations in the bulk sample and constituent minerals, which is likely more accurate than point counting. It is possible that mineral mode in the starting mantle is not uniform. In this study, we consider three mineral modes for the starting mantle source. For simplicity, we fix the modal abundance of olivine in the mantle source to 56% and vary the cpx:opx proportion in the mantle source (Fig. 3). This is a reasonable approach as (1) the relative REE pattern in the bulk rock is not very sensitive to the abundance of olivine in the mantle source, and (2) the resultant residual modes cover a wider range of mineral modal abundances (Fig. 3). Finally, the grain size of the starting mantle is unknown, although in general grain size of opx is larger than grain size of cpx in peridotites. As a starting

model, we assume that the grain size ratio between opx and cpx ($\frac{d_{cpx}}{d_{opx}}$) does not change during melting. The latter helps to simplify the evaluation of the relative diffusion rate between opx and cpx (Eq. 2).

Since there is no analytical solution to the multi-mineral disequilibrium melting model (Eqs. A2a-A2c in Appendix A), we use Markov chain Monte Carlo (MCMC) method to invert for the melting parameters F, ε_{cpx}^{1300}, and $\mathbb{R}$. MCMC methods are a class of powerful statistical tools for solving nonlinear inverse problems (e.g., Sambridge and Mosegaard, 2002). Liu and Liang (2017) used MCMC to invert melting parameters from REE abundance in residual cpx in abyssal peridotites. To facilitate MCMC inversion, we set bounds for the disequilibrium parameter ε_{cpx}^{1300} to [0, 0.15] and the melt suction rate $\mathbb{R}$ to [0, 1], based on previous inversion results using similar model or method (Lundstrom, 2000; Liang and Peng, 2010; Liang and Liu, 2016; Liu and Liang, 2017). We run 10,000 to 50,000 simulations for each sample to ensure convergence and use the result to calculate best fitting parameters and uncertainties. The best fitting parameters are then used to calculate REE abundances in the bulk sample, residual cpx and opx, and chemically re-equilibrated cpx and opx at subsolidus temperatures. Below we present results from two case studies.

3.1. Case 1: Mantle xenoliths

To demonstrate the basic feature of the multi-mineral disequilibrium melting model and the effect of subsolidius redistribution, we select 9 well-characterized spinel lherzolite and harzburgite xenoliths from the literature: 3 samples from Yangyuan, North China Craton (Liu et al., 2012), 1 sample from West Eifel, Germany (Witt-Eickschen and O'Neill, 2005), 1 sample from East Africa Rift (Bedini and Bodinier, 1999), 3 samples from Kilbourne Hole, New Mexico (Harvey et al., 2012), and 1 sample from the Coast Ranges of central California (Quinn et al., 2018). These samples are protogranular, free of garnet, plagioclase, hydrous minerals, and veins. They are selected on the basis of their depleted light REE patterns in cpx and opx, well-defined linear trends for at least the middle and heavy REE in the inversion diagram of the REE-in-two-pyroxene thermometer, and similar equilibrium temperatures between major element-based and REE-based pyroxene thermometers. Figure 2 shows that the calculated temperatures are generally below the solidus of the peridotite xenoliths. Figure 3a displays modal abundances of the selected

samples. For reference, we plot selected major element concentrations in these samples as a function of bulk MgO content and spinel Cr# (= 100Cr/Cr+Al, in molar) in supplementary Figs. S3a and S3b. Supplementary Tables S1b and S2 and Fig. S5 present results of MCMC simulations with PM and DMM starting compositions for the nine xenolith samples along the 1300°C mantle adiabat (Fig. S1). Figure 4 shows an example of MCMC simulations for sample CK-2 from the Coast Ranges of central California (Quinn et al., 2018). The main results are summarized below.

First, the bulk REE patterns are well reproduced by the multi-mineral disequilibrium melting model. The quality of fit is not very sensitive to the choice of starting mantle mode (cf. Figs. 4a-4c). This is shown by the similar Pearson's Chi-squares among the three cases for each sample (Supplementary Table S2). Here we calculate Pearson's Chi-square for the bulk REE after inversion using the expression:

$$\chi^2_{bulk} = \sum_{j=1}^{N} \frac{\left(C_{s,j} - C^m_{s,j}\right)^2}{C_{s,j}}, \quad (7)$$

where $C_{s,j}$ and $C^m_{s,j}$ are the model-derived and measured bulk solid concentrations for element j, respectively; N is the number of elements in the model. In general, the smaller the Pearson's Chi-square, the better the predict model will be. There is a small trade-off between cpx abundance in the starting mantle and the degree of melting: the higher the cpx mode in the starting mantle, the greater the degree of melting is required to match the observed depletion in REE in the bulk residue. Increasing cpx mode from 14% to 20% in the starting mantle results in 0.11~3% increase in the inferred degree of melting for the nine xenolith samples.

Second, the observed REE patterns in residual cpx and opx (filled blue and green circles in Fig. 4) cannot be reproduced directly using melting parameters derived from the bulk REE pattern (blue and green solid lines). Very often, LREE in opx is overestimated and HREE in cpx is underestimated by the melting model, which appears to be consistent with the subsolidus reequilibration trends displayed in Fig. 1a. To quantify the effect of subsolidius redistribution, we recalculated the model-derived REE abundances in opx and cpx using the temperature and major element composition dependent REE opx-cpx partition coefficients (Sun and Liang, 2014) and closure temperatures (T_{REE}) derived from the REE-in-two-pyroxene thermometer (Liang et al., 2013). The latter is 964°C for sample CK-2. Figure 4 and supplementary Fig. S5 show that the

matches to the measured REE patterns in cpx and opx in the nine xenolith samples are considerably improved after adjustment of subsolidus redistribution. This is an important result from this study.

Finally, for a given sample, our preferred starting mantle mode and melting parameter should have the smallest sum of Pearson's Chi-squares for the bulk peridotite, cpx, and opx among the three starting mantle modes, where Pearson's Chi-squares for cpx and opx are calculated after adjustment for subsolidus reequilibration. Supplementary Table S2 lists melting parameters of our preferred model. It is interesting to note that the quality of fit to REE patterns in cpx is comparable to that based on inversion of REE in cpx alone, as the calculated Pearson's Chi-squares for cpx from the bulk model and cpx alone model are very similar for the nine samples (Supplementary Table S2). The misfits, if present, are mostly LREE in opx and cpx. (We will discuss the misfits in Section 4.) Figure 4 and supplementary Fig. S5 also show that the recalculated REE patterns in model-derived opx and cpx (dashed lines) are sensitive to starting mantle mode. This is highlighted by the large differences in the sum of Pearson's Chi-squares among the three choices of mantle mode (e.g., 0.94, 4.25, and 15.2 for 14%, 17%, and 20% cpx in the starting mantle, respectively for sample CK-2). Hence by modeling REE redistribution among cpx, opx, and olivine in the mantle xenolith after melting, it is possible to constrain mineral mode of the starting mantle.

3.2. Case 2: Abyssal peridotites

Trace element abundances in cpx in abyssal peridotites have been widely used to study melting and melt-rock interaction processes beneath mid-ocean ridges (e.g., Johnson et al., 1990; Kelemen et al., 1997; Hellebrand et al., 2002, 2005; Salters and Dick, 2002; Hellebrand and Snow, 2003; Brunelli et al., 2006; Warren et al., 2009; Brunelli and Seyler, 2010; D'Errico et al., 2016). Detailed modeling of REE patterns in residual cpx in abyssal peridotites from Central Indian Ridge (data from Hellebrand et al., 2002) using an equilibrium near fractional melting model revealed a systematic difference between measured and calculated HREE in cpx: very often model predicted HREE in cpx are slightly lower than those measured in actual samples (see Fig. 8 in Liang and Peng, 2010). To fit the HREE in cpx, one can decrease the extent of melting, but this would result in an over estimation of LREE in cpx. One way to get around this dilemma is by allowing small extent of chemical disequilibrium for LREE in cpx (Liang and Liu, 2016; Liu and Liang, 2017), which hinders the depletion of LREE in cpx. This is consistent with measured rates of REE diffusion in diopside (Van Orman et al., 2002). Another possible way to elevate HREE in cpx is

through subsolidus reequilibration, as we demonstrated in previous sections. However, the extent of subsolidus redistribution may be limited due to higher REE closure temperatures recorded in abyssal peridotites (Fig. 2) (Liang et al., 2013; Dygert and Liang, 2015; Yao and Liang, 2015). Yet another mechanism to produce depleted LREE and elevated HREE in cpx is to start melting in the garnet stability field (e.g., Johnson et al., 1990; Hellebrand et al., 2002; Brunelli et al., 2006).

To critically assess the roles of garnet field melting, finite rate of chemical exchange for LREE, and subsolidus redistribution of REE between cpx and opx in affecting REE patterns in abyssal peridotites, we select 12 residual abyssal peridotites from the literature that reported REE abundances in both cpx and opx: 4 samples from eastern Southwest India Ridge (SWIR, Selyer et al., 2011), 2 samples from Gakkel Ridge (D'Errico et al., 2016), 4 samples from western SWIR (Warren et al., 2009), and 2 samples from Central Atlantic Ridge (Brunelli and Seyler, 2010). Based on the criteria of Warren (2016), these samples are residual peridotites as they are free of plagioclase and melt veins, have low TiO_2 in spinel and LREE deplete REE patterns in cpx and opx. Similar to mantle xenoliths, these samples also have well-defined linear trends for at least the middle and heavy REE in the inversion diagram of the REE-in-two-pyroxene thermometer. Fig. 3b display modal abundances of the selected samples. For reference, we also plot major element compositions of the samples as a function of bulk MgO content and spinel Cr# in supplementary Figs. S4a and S4b. Previous experimental studies have demonstrated that melting reaction of peridotite varies systematically with pressure (e.g., Kinzler and Grove, 1992; Baker and Stolper, 1994; Walter and Presnall, 1994). During decompression melting of garnet lherzolite, modal abundance of opx first increases until the pressure is around 2 GPa and then decreases as the pressure decreases (Ghiorso et al., 2002; Walter, 2014). To include more realistic melting reaction for decompression melting, we use pMELTS (Ghiorso et al., 2002) to calculate mineral mode along an adiabatic melting path that has a potential temperature of 1330℃. The starting mantle contains 150 ppm water. In this pMELTS-based model, the maximum extent of melting in the garnet stability field is 0.7% and the cpx exhausts at $F = 20\%$. Since there is no clear experimental nor geophysical evidence for the presence of high-porosity channels at depth greater than 60 km beneath mid-ocean ridges, we use the batch melting model for melting in the garnet stability field (i.e., by setting $\mathbb{R} = 0$ in our model). Fig. 3b displays variations of mineral mode in residual peridotites calculated using pMELTS for three choices of starting mantle mineralogy (solid curves). Supplementary Fig. S6 and Supplementary Tables S1c and S2 present simulation results for

individual samples. Figure 5 shows an example of MCMC simulations for sample Van 7-85-49 from Western SWIR (Warren et al., 2009). The main results are summarized below.

Similar to the case of mantle xenolith, the multi-mineral disequilibrium melting model can fit the bulk REE patterns very well for most of the abyssal peridotite samples included in this study. The exceptions are sample Van7-96-38 from Western SWIR (Warren et al., 2009) and sample Dr 23-3-2 from Eastern SWIR (Seyler et al., 2011) which exhibit some misfits in light and middle REE (Fig. S6). We will discuss the misfits in Section 4.1. As in the case of mantle xenolith, the quality of fit to the bulk REE data is not very sensitive to the starting mantle mode, and the match to the measured REE in cpx and opx depends strongly on the starting mantle mode (cf. the three cases in Fig. 5). Overall, the fits to the observed REE patterns in cpx and opx are improved after adjustment of subsolidus redistribution (cf. solid and dashed lines in Fig. 5 and Fig. S6). However, the improvement is moderate because of the relatively high T_{REE} for the peridotite samples (Fig. 2) and very small adjustment for REE in cpx. These are consistent with the simply analysis of Sun and Liang (2014) and the inferred thermal history of abyssal peridotites (Liang et al., 2013; Dygert and Liang, 2015; Yao and Liang, 2015). Supplementary Table 2 lists melting parameters of our preferred model for the 12 abyssal peridotite samples based on the sum of Pearson's Chi-squares of the bulk and subsolidus redistributed cpx and opx.

4. DISCUSSION

4.1. Misfits of REE in the bulk samples

Although the multi-mineral disequilibrium melting model can account for most of the variations of REE + Y in the bulk peridotites, noticeable misfits in the light and middle REE are observed in samples Van7-96-38 (from Western SWIR, Warren et al., 2009) and Dr23-3-2 (from eastern SWIR, Seyler et al., 2011, see Fig. S6). In both cases, the model-predicted La, Er, Tm and Yb in the bulk residue are higher than, whereas the predicted Nd, Sm, E, Gd and Tb are lower than, measured values in the samples. This humped feature is not sensitive to starting mantle mode, and is also present in the cpx-alone inversion models. Addition of melt would elevate La in cpx and opx and hence cannot explain the depleted LREE patterns in the two samples. The lower than expected bulk La, Er, Tm and Yb can be accounted for by increasing the degree of melting, but

this would result in additional misfits in Nd, Sm, E, Gd and Tb. Since partition coefficients of middle REE in cpx are higher than those in garnet and the partition coefficients of HREE in cpx are lower than those in garnet, prolonged melting in the garnet stability field can produce the humped middle REE pattern in cpx and the bulk residue (e.g., Johnson et al., 1990). Our pMELTS based model for abyssal peridotites presented in Section 3.2 includes 0.7% initial melting in the garnet field. To further explore the role of garnet field melting, we consider a hypothetic case in which batch melting in the garnet stability field is 4.1%. Supplementary Fig. S7 presents the simulation results. The simulated bulk rock and pyroxene REE patterns after 4.1% batch melting in the garnet field show only a small improvement for sample Dr23-3-2 (the sum of Pearson's Chi-squares decreases from 3.8 to 3.3 which is still higher than the other 10 abyssal peridotites) and no improvement at all for sample Van7-96-38. Hence the misfits are unlikely due to batch melting in the garnet stability field. Although fractional melting of garnet lherzolite can produce humped REE in cpx (Johnson et al., 1990), the physical mechanism for fractional melting in the garnet stability field remains uncertain.

Abyssal peridotites are heavily altered by serpentinization. It is possible that mineral modes in these two samples are not accurately determined. To explore this possibility, we reconstruct two new modal abundances for the two samples: one by increasing cpx mode by 2% and decreasing opx mode by 2%, and the other by decreasing cpx mode by 2% and increasing opx mode by 2%. We run MCMC simulations followed by subsolidus redistribution for these 4 cases and the results are shown in supplementary Fig. S8. Changing cpx mode by ±2% in the samples does not lead to a significant improvement in the fit to the reconstructed bulk REE in these two samples (i.e., the humped pattern persists). However, addition of 2% cpx does result in moderate improvement in the match to the observed REE patterns in cpx and opx in the two samples. This is confirmed by the smaller sum of Pearson's Chi-squares for the +2% cpx case.

We should point out that none of the hypotheses explored in this section can explain the humped REE pattern in cpx using the cpx-alone inversion model. In theory, one can match the observed REE pattern in bulk residue by judiciously adjusting starting mantle composition. It is possible that composition of the starting mantle for these two samples are different from DMM. We will come back to this point in Section 4.3.

4.2. Misfits of LREE in opx and cpx: Incomplete reequilibration?

A common misfit shared by all the abyssal peridotite samples and four of the nine mantle xenoliths (ET80, CK-2, YY-26B, and KN03-25) in this study is that model-derived LREE (La + Ce + Pr ± Nd) are lower in cpx but higher in opx than measured values in cpx and opx, respectively. The misfit, which persists even after adjustment of subsolidus re-distribution, can be visualized by plotting the apparent opx/cpx REE partition coefficient against REE ionic radius: the apparent partition coefficients for the middle and heavy REE follow closely to an isotherm, whereas those for LREE are gradually displaced above the isotherm, defining a spoon-shaped or U-shaped pattern (Figs. 6a and 6b). In the inversion diagram for the REE-in-two-pyroxene thermometer, the displaced LREE fall below the linear trend established by the heavy and middle REE and are excluded from the temperature calculation (Liang et al., 2013). Spoon- or U-shaped opx/cpx REE partitioning pattern is a common feature among mantle samples (e.g., Stosch, 1982; Agranier and Lee, 2007; Seyler et al., 2011). It arises when LREE in opx and cpx are out of chemical equilibrium. Agranier and Lee (2007) identified two mechanisms that can produce U-shaped disequilibrium patterns in mantle xenoliths from Dish Hill, California and abyssal peridotites from the Gakkel Ridge: diffusive fractionation at subsolidus state or metasomatism introduced by "injection and subsequent freezing in of small amounts of melt" under lithospheric or asthenospheric conditions. These authors preferred the latter mechanism as they argued that diffusive fractionation alone could not account for the large deviation in the apparent opx/cpx LREE partition coefficients in some samples. The 9 mantle xenoliths and 12 abyssal peridotite samples included in the present study are all depleted in LREE. Given that our multi-mineral disequilibrium melting model can fit the bulk REE patterns very well in these samples, we can rule out the melt addition hypothesis for these samples.

We suggest that the spoon- or U-shaped opx/cpx REE partitioning patterns can be produced by disequilibrium melting followed by diffusive exchange between cpx and opx at subsolidus state. Figures 6a and 6b compare the apparent opx/cpx REE partition coefficients calculated from the measured REE abundances in opx and cpx in mantle xenolith CK-2 from the Coast Ranges of central California (Quinn et al., 2018, filled circles) and abyssal peridotite Van7-85-49 from western SWIR (Warren et al., 2009) with those calculated using melting parameters derived from our MCMC simulations (magenta lines). (Similar plots for other samples included in this study are presented in supplementary Figs. S5 and S6.) In both samples, the simulated apparent partition coefficients at the end of melting are displaced above the measured values. Since opx/cpx REE

partition coefficients decrease with the decrease of temperature (cf. the three isotherms in Fig. 6) and diffusion coefficients of REE in cpx increase systematically from La to Lu at a given temperature (Van Orman et al., 2001, 2002; see also supplementary Fig. S1c), time scales for diffusive exchange between opx and cpx in a closed system are longer for LREE than HREE (see Fig. 5 in Liang, 2014). During diffusive reequilibration, HREE approach opx/cpx equilibrium partitioning faster than LREE. Depending on thermal history experienced by the samples (e.g., cooling and upwelling rates), the elevated opx/cpx REE patterns produced by disequilibrium melting (magenta lines in Fig. 6) would be gradually relaxed to the spoon-shaped pattern recorded in the peridotite samples (filled circles). As a proof-of-concept, we carry out two forward simulations of diffusive reequilibration of REE between opx and cpx under two prescribed cooling rates. In this simple demonstration, cooling starts at the end of melting and terminates at the closure temperature of REE (i.e., $T = T_{REE}$). Figures 6a and 6b show that the results are promising (thin orange lines). In a more complicate but realistic situation, the cooling rate, which is likely very different for the mantle xenolith and abyssal peridotite, may vary as a function of time. Hence it may be possible to deduced cooling rate through detailed modeling of the spoon-shaped opx/cpx REE patterns in residual peridotites, a subject that we will pursue in the near future.

4.3. Mantle source composition

The starting mantle composition (DMM vs. PM) affects our inversion results. The depleted MORB mantle or DMM (e.g., Workman and Hart, 2005) has been widely used in REE modeling of abyssal peridotites. In their original studies of mantle xenoliths, Liu et al. (2012) and Harvey et al. (2012) anchored their major and trace element data to the primitive mantle of McDonough and Sun (1995), whereas Quinn et al (2018) used DMM and HREE in their samples to infer the extent of melting. We used the primitive mantle of McDonough and Sun (1995) as the starting mantle composition in our inversion of the mantle xenolith data. Composition of the mantle source is unlikely homogeneous, even for a suite of depleted samples from the same locality. Liu et al. (2012) reported Nd and Hf isotopic compositions of cpx for the three North China Craton samples (YY-26, YY-40B, and YY-42) included in this study. They found that samples YY-40B and YY-42 have considerably higher $^{143}Nd/^{144}Nd$ and $^{176}Hf/^{177}Hf$ ratios than sample YY-26 and suggested that samples such as YY-26 might be affected by melt addition via melt-rock interaction. In Section 3.1, we showed that REE patterns in the bulk sample, cpx, and opx in YY-26 can be well

reproduced by our melting followed by subsolidus reequilibration model using PM as the starting mantle composition (Fig. S5). The misfit is LREE in opx, which is likely resulted from incomplete reequilibration at a low temperature (T_{REE} = 889 °C). The higher $^{143}Nd/^{144}Nd$ and $^{176}Hf/^{177}Hf$ ratios in samples YY-40B and YY-42 suggest that these samples may have derived from a more depleted mantle source. To test this hypothesis, we run MCMC simulations for samples YY-40B and YY-42 using DMM as our starting mantle composition. The results are summarized in Supplementary Table S2 and Fig. S5: the fits to sample YY-40B are slightly improved as the sum of Pearson's Chi-squares decreases from 1.76 (PM) to 1.68 (DMM), whereas no improvement is observed for YY-42 as the sum of Pearson's Chi-squares increases from 0.62 (PM) to 1.21 (DMM). In fact, inversion of the remaining 7 xenolith samples with DMM starting composition leads to moderate to significant reduction in the quality of fits to the observed REE patterns (i.e., the sum of Pearson's Chi-squares has increased, Fig. S5). This intriguing result suggests that composition of PM is more suitable for modeling REE depletion in residual mantle xenoliths, although the number of samples included in this study is rather small. Given the slight improvement of fits to sample YY-40B using DMM starting mantle composition, we include inversion results with DMM starting composition in our discussion (two points connected by red dashed lines in Figs. 7a, 8a, 8c, and 9 below).

Composition of the average DMM is a convenient common start point in modeling REE depletion in abyssal peridotites. According to Warren et al. (2009), $^{143}Nd/^{144}Nd$ ratios in cpx in the 4 samples from SWIR (Van7-85-42, Van7-85-47, Van7-85-49, and Van7-96-38) are more similar to the depleted endmember of DMM (D-DMM) of Workman and Hart (2005) than the average DMM (see Fig. 5a in Warren et al., 2009). Intrigued, we run MCMC simulations again for the 4 samples using REE + Y in the D-DMM of Workman and Hart (2005) as starting mantle composition. The results are presented in supplementary Fig. S9: the fits to the observed REE in the bulk, cpx, and opx are slightly improved as the sums of Pearson's Chi-squares for the 4 samples are all reduced. The small improvement is probably due to the fact that concentration differences between D-DMM and DMM of Workman and Hart (2005) are small. As we discussed in Section 4.1, concentrations of Pr to Eu in sample Van7-96-38 are underestimated in our models. It is possible that the starting mantle for Van7-96-38 is more depleted than D-DMM. Existence of ultra-depleted mantle domains have been proposed for magma genesis beneath mid-ocean ridges based on Os, Nd, and Hf isotope ratios in residual peridotites and olivine-hosted melt inclusions (e.g., Liu et al., 2008; Stracke et al., 2011, 2019; Sanfilippo et al., 2019). The mantle source composition

for residual abyssal peridotites such as the ones examined in this study is likely more variable than that represented by the DMM model of Workman and Hart (2005). More study is needed to quantify the abundances of REE and other trace elements in these extremely depleted mantle sources.

4.4. Mantle source mode

The starting mantle mode also affects fitting results. Our original purpose of exploring 3~6% variations in cpx and opx modes in the starting lherzolitic mantle was to understand the large variations in mineral modal abundance observed in the mantle xenoliths and abyssal peridotites included in this study, as such variations cannot be produced by melting a single mantle source. It turns out that the quality of fits to the bulk REE in the mantle xenoliths and abyssal peridotites are not very sensitive to the starting mantle mode, albeit a trade-off between cpx mode in the starting mantle and the inferred degree of melting (Section 3.1). This is explained by the very similar bulk REE partition coefficients for the three starting mantle modes: they are subparallel to each other in the spider diagram (see supplementary Fig. S10). Hence one cannot use bulk REE in residual peridotite to discriminate starting mantle mode. However, REE abundances in residual cpx and opx are sensitive to starting mantle mode for the mantle xenoliths and abyssal peridotites. This is due simply to mass balance and temperature-dependent opx/cpx and ol/cpx REE partition coefficients (Eqs. 5 and 6). During subsolidus reequilibration in a closed system (i.e., for a constant C_s in Eq. 5), concentrations of REE in opx and ol in lherzolite or harzburgite decrease with the decrease of temperature, whereas concentrations of REE in cpx increase. At a given temperature, the change of concentration depends on mineral mode (see Fig. 6 in Sun and Liang, 2014) which is sensitive to the starting mantle mode and the melting reaction. During subsolidus reequilibration, cpx and opx modes and major element compositions also change due to pyroxene exsolution and subsolidus reaction among the mantle minerals, which complicates the application of Eq. 6. A preliminary pMELTS-based study suggests that these major element effects are small to moderate on REE re-distribution in peridotites (Yao, 2015). Results from this study suggest that the mineral mode in the starting mantle is not homogeneous. This is consistent with the scattered correlations between the bulk MgO and incompatible major and minor elements (CaO, Al_2O_3, Na_2O, and TiO_2) in the mantle xenoliths and abyssal peridotites (supplementary Figs. S3a and S4a).

4.5. Comparing melting parameters derived from REE in the bulk and REE in cpx

In general, degrees of melting based on MCMC inversion of REE + Y in the bulk samples (designated as F_{bulk} hereafter) and cpx alone (F_{cpx}) are positively correlated (Fig. 7). Figure 7a compares our estimated F_{bulk} with F_{cpx} for the nine xenoliths. Samples CK-2 (Coast Ranges of central California, Quinn et al., 2018) and ET80 (East African Rift, Bedini and Bodinier, 1999) are considerably more fertile in terms of spinel Cr# and contain 12.4% and 15.8% cpx, respectively. Hence REE + Y in cpx in these two samples should be less affected by subsolidus redistribution. Indeed, the calculated degrees of melting for CK-2 and ET80 based on the multi-mineral disequilibrium melting model (3.7% and 3.9%) are essentially the same as that derived from HREE in cpx (2.9% and 4.2%, Supplementary Table S2). Nonetheless, light and middle REE in opx in these samples are strongly affected by subsolidus redistribution, which is consistent with their low T_{REE} (964°C and 952°C, respectively). The remaining seven samples are more depleted. Except sample YY-42, their inverted F_{bulk} are 2~6% higher than F_{cpx}. Sample YY-42 from North China Craton (Liu et al., 2012) has the lowest cpx mode (4%, a harzburgite), the highest spinel Cr#, and the second highest F_{bulk} (19%) among the nine xenolith samples included in this study. This is in contrast to the rather small F_{cpx} for this sample (11%, Table S2). Given its very refractory nature, we suspect that a large fraction of cpx in this sample may have derived from exsolution of opx after melting. Hence the degree of melting inferred from cpx alone in this sample is not meaningful. Caution should be exercised when inferring extent of melting using REE abundance in cpx in harzburgitic mantle xenoliths.

Given the relatively high T_{REE} recorded by the 12 abyssal peridotite samples (Fig. 2) and the limited extent of subsolidus redistribution of REE between cpx and opx (Section 3.2), it is not surprising that the inferred degrees of melting based REE in the bulk samples are only slightly higher than those derived from REE in cpx alone (Fig. 7b). The maximum difference is only 2.2%, which is in general agreement with the assessment of Sun and Liang (2014). Hence in the absence of bulk REE data, one can use REE in cpx to infer the extent of melting experienced by residual abyssal peridotites.

There are considerable uncertainties in the inverted disequilibrium parameter for La in cpx (ε_{cpx}^{1300}) and the melt suction rate ($\mathbb{R}$) (Supplementary Table S2). Excluding melting parameters from cpx-alone inversion for sample YY-42, inverted disequilibrium parameters for La in cpx derived from REE in the bulk and REE in cpx alone are correlated, whereas the melt suction rates

584 are uncorrelated for the eight mantle xenoliths (Figs. 8a and 8c). It also appears that inverted
585 disequilibrium parameter for La in cpx and melt suction rate derived from REE in the bulk are
586 lower than values derived from REE in cpx alone for the abyssal peridotites (Figs. 8b and 8d),
587 although exceptions are noted (sample Dr23-3-2). Potential causes for the apparent differences
588 between the xenolith and abyssal peridotite samples include difference in tectonic setting (i.e.,
589 thermal and magmatic histories), difference in melting path and melting reaction, and/or nonlinear
590 trader-off between the two melting parameters in the presence of inaccurate trace element data.
591 More work is needed to confirm and sort out the differences noted.

592 **4.6. Variations of the melting parameters derived from bulk REE with key melting indices**

593 Chromian spinel has been widely used in studies of abyssal peridotites and peridotites from
594 other tectonic settings (e.g., Dick and Bullen, 1984). Hellebrand et al (2001) showed that spinel
595 Cr# in residual abyssal peridotites are strongly and inversely correlated with HREE abundances in
596 cpx in the peridotites and developed empirical equations relating degree of melting to spinel Cr#
597 for abyssal peridotites. Figure 9a shows the positive correlation between our inverted F_{bulk} and
598 spinel Cr# for the xenolith and abyssal peridotite samples included in this study. The abyssal
599 peridotites are bracketed by the batch melting and perfect fractional melting trends of Hellebrand
600 et al. (2011). However, due to the low spinel Cr#, the mantle xenolith data are mostly plotted below
601 the batch melting trend. The latter may in part due to subsolidus redistribution of Cr and Al in
602 spinel peridotite (e.g., Viogt and von der Handt, 2011). Caution should be exercised when inferring
603 extent of melting using Cr# of spinel in mantle xenoliths.

604 Our inferred degrees of melting for the mantle xenoliths and abyssal peridotites are
605 consistent with the observed variation trends of the major and minor elements in the samples. For
606 example, with increasing degree of melting, MgO content in the bulk residue increases from the
607 starting DMM or PM (Fig. 9b), whereas CaO, Al_2O_3, Na_2O, and TiO_2 contents in the bulk sample
608 decrease (Figs. S3c and S4c). The scatteredness of the data shown in Figs. 9b, S3c and S4c can be
609 attributed to variations in mineral modes, hence major element composition, in the starting mantle.

610

611 **5. What have we learned from REE abundances in residual peridotites?**

LREE depleted spinel peridotites are generally interpreted as residues of mantle melting. Through case studies of carefully selected residual spinel peridotites from two distinct tectonic settings we have demonstrated the advantages of using REE abundances in both the bulk rock and constituent minerals (cpx and opx) in deducing magmatic and thermal history of the peridotites. REE abundances in bulk residual peridotites are well-suited for studying melting process, provided their concentrations are accurately determined, and grain size and mineral mode are known. As a first application, we kept opx and cpx grain size ratio constant in our MCMC inversion. This is likely a simplification, as we do not know how grain sizes of cpx and opx vary during mantle melting and subsolidus reequilibration. LREE in opx and HREE in cpx are more susceptible to subsolidus redistribution. The extent of redistribution depends on cpx and opx abundances in the sample and thermal history experienced by the peridotite. We have shown that, by modeling subsolidus redistribution of REE between opx and cpx after melting, it is possible to discriminate mineral mode of the starting mantle. HREE in cpx in less primitive spinel lherzolite and harzburgite from continental cratons are significantly reset by subsolidus reequilibration over geologic time. We do not recommend the use of REE in cpx alone to study mantle melting process in such samples. The harzburgite YY-42 from North China Craton (Liu et al., 2012) is an extreme example. In the absence of REE abundance in opx, REE in cpx in residual abyssal peridotites can be used to infer the degree of melting of samples that experienced small to moderate extent of melting. HREE in highly depleted harzburgite may be affected by subsolidus reequilibration. By modeling REE abundances in the bulk and constituent cpx and opx, it is also possible to discriminate starting mantle composition. We find that composition of the primitive mantle is more suitable for modeling REE depletion in cratonic mantle xenoliths, whereas composition of DMM is more suitable for modeling REE depletion in residual abyssal peridotites. REE patterns in some of the isotopically more depleted abyssal peridotites such as the four samples from SWIR (Warren et al., 2009) can be better explained by a starting mantle that is more depleted than the average DMM.

The mantle xenoliths and residual abyssal peridotites examined in this study are a small fraction of xenolith samples (9 out of 71) and abyssal peridotite samples (12 out of 60) analyzed in the original studies cited in Sections 3.1 and 3.2. To focus on REE depletion in the bulk peridotite produced by partial melting, we exclude samples that have LREE enriched patterns, samples that may have been affected by melt addition, and samples that exhibit disequilibrium

partitioning in HREE between opx and cpx. In spite of our conservative approach in sample selection, we find that the composition and mode of the starting mantle are still not homogeneous for these two groups of highly selective mantle peridotites. It is well known that the upper mantle is chemically (e.g., enriched vs. depleted) and lithologically (e.g., peridotite vs. pyroxenite) heterogenous. Results from the present study suggests that the endmember of the depleted peridotitic upper mantle is also modally heterogeneous. A modally heterogeneous starting mantle provides a simple explanation for the large variations of mineral mode observed in peridotitic mantle xenoliths and abyssal peridotites, and may have important implications for the interpretation of geophysical data.

Finally, we note that the methodology developed in this study can also be applied to other trace elements in residual peridotites, provided their diffusion in and partitioning between mantle minerals are well characterized. A potential target is the high field strength elements. Spoon- or U-shaped opx/cpx REE partitioning patterns are observed in all the abyssal peridotite samples included in this study. Four of the nine mantle xenoliths that have lower REE closure temperature also have spoon-shaped REE partitioning pattern. Through simple forward modeling, we have shown that the spoon- or U-shaped opx/cpx REE partitioning patterns can be produced by disequilibrium melting followed by diffusive exchange between cpx and opx at subsolidus state. It may be possible to deduce cooling rate and thermal history through detailed modeling of spoon-shaped opx/cpx REE partitioning patterns in mantle samples.

ACKNOWLEDGEMENTS

We thank Daniele Brunelli, Henry Dick, Jingao Liu, and Jessica Warren for useful discussion regarding grain size in peridotites. This work was supported by National Science Foundation grant EAR-1852088 and the China Scholarship Council (201806010079).

APPENDIX A. GOVERNING EQUATIONS

The non-modal disequilibrium melting model of Liang and Liu (2016) is intended for modeling trace element fractionation during concurrent melting, channelized melting extraction, and finite rate of crystal-melt chemical exchange in an upwelling steady-state melting column. In terms of the degree of melting experienced by the solid matrix (F), mass conservation equations for a trace element in the interstitial melt (C_f), residual solid (C_s), individual mineral (C_s^j) can be written as:

$$\varepsilon_{cpx}(1-\mathbb{R})F\frac{\mathrm{d}C_f}{\mathrm{d}F} = \varepsilon_{\mathrm{cpx}}\left(C_s^p - C_f\right) + \sum_{j=1}^{N} w_j \frac{R_j}{R_{cpx}}\left(C_s^j - k_j C_f\right) \qquad (A1a)$$

$$\varepsilon_{cpx}\ (1-F)\frac{\mathrm{d}C_s}{\mathrm{d}F} = \varepsilon_{cpx}\left(C_s - C_s^p\right) - \sum_{j=1}^{N} w_j \frac{R_j}{R_{cpx}}\left(C_s^j - k_j C_f\right) \qquad (A1b)$$

$$\varepsilon_{\mathrm{cpx}}\,(1-F)\frac{\mathrm{d}C_s^j}{\mathrm{d}F} = -\frac{R_j}{R_{cpx}}\left(C_s^j - k_j C_f\right) \qquad (A1c)$$

where k_j is the partition coefficient between mineral j and melt for the element of interest; $\mathbb{R}$ is the dimensionless melt suction rate defined as the fraction of melt removed from the residual solid (to a nearby channel) relative to the amount of melt produced by melting (Iwamori, 1994; Liang and Peng, 2010); ε_{cpx} is the disequilibrium parameter for a trace element in cpx; C_s^p is the concentration of bulk solid calculated according to melting reaction; and w_j is the weight fraction of mineral j in residual solid. The latter three parameters are defined as follows:

$$\varepsilon_{\mathrm{cpx}} = \frac{\Gamma}{\rho_s(1-\phi_f)R_{cpx}} \qquad (A1d)$$

$$C_s^p = \sum_{j=1}^{N} w_j^p C_s^j \qquad (A1e)$$

$$\mathrm{w_j} = \frac{w_j^0 - w_j^p F}{1-F} \qquad (A1f)$$

where Γ is the melting rate; ρ_s is the density of the bulk solid; ϕ_f is the volume fraction of the melt in the residue; w_j^0 is the weight fraction of mineral j at the onset of the melting; and w_j^p is the weight fraction of mineral j participating in the melting reaction. Equations (A1a)-(A1c) can be further simplified by assuming that the interstitial melt and olivine and spinel are location chemical equilibrium. The mass conservation equations become:

$$\left(\varepsilon_{\mathrm{cpx}}(1-\mathbb{R})F+\varepsilon_{\mathrm{cpx}}(1-F)\left(w_{ol}k_{ol}+w_{sp}k_{sp}\right)\right)\frac{\mathrm{d}C_f}{\mathrm{d}F}=$$

$$\varepsilon_{\mathrm{cpx}}\left(C_s^p-C_f\right)+w_{cpx}\left(C_s^{cpx}-k_{cpx}C_f\right)+w_{opx}\frac{R_{opx}}{R_{cpx}}\left(C_s^{opx}-k_{opx}C_f\right) \quad \text{(A2a)}$$

$$\varepsilon_{\mathrm{cpx}}(1-F)\frac{\mathrm{d}C_s^{cpx}}{\mathrm{d}F}=-\left(C_s^{cpx}-k_{cpx}C_f\right) \quad (A2b)$$

$$\varepsilon_{\mathrm{cpx}}(1-F)\frac{\mathrm{d}C_s^{opx}}{\mathrm{d}F}=-\frac{R_{opx}}{R_{\mathrm{cpx}}}\left(C_s^{opx}-k_{opx}C_f\right) \quad (A2c)$$

$$C_s^p=\ w_{cpx}^pC_s^{cpx}+w_{opx}^pC_s^{opx}+w_{ol}^pk_{ol}C_f+w_{sp}^pk_{sp}C_f \quad (A2d)$$

Concentration of REE in the bulk residue can be calculated using the expression:

$$C_s=\sum w_jC_s^j\ =\ w_{cpx}\,C_s^{cpx}+w_{opx}\,C_s^{opx}+w_{ol}\,k_{ol}C_f+w_{sp}\,k_{sp}C_f \quad (A2e)$$

Equations (A2a)-(A2c) are closed by the following boundary conditions at the bottom of the melting column ($F = 0$):

$$C_f(0)=\frac{\varepsilon_{\mathrm{cpx}}\,k_p+k_0}{k_0\left(\varepsilon_{\mathrm{cpx}}+k_0\right)}C_s^0 \quad (A2f)$$

$$C_s^{cpx}(0)=\frac{k_{cpx}}{k_0}\,C_s^0 \quad (A2g)$$

$$C_s^{opx}(0)=\frac{k_{opx}}{k_0}C_s^0 \quad (A2h)$$

where k_0 is the bulk solid–melt partition coefficient at the onset of melting; and k_p is the bulk solid–melt partition coefficient according to the melting reaction. Equation (A2f) is based on the analysis of Liang and Liu (2016). Equations (A2a)-(A2c) are a set of coupled ordinary differential

equations and can be solved numerically using standard methods. In this study, we solve these equations using the routine ODEIENT in Python.

References

Agranier A. and Lee C. T. A. (2007) Quantifying trace element disequilibria in mantle xenoliths and abyssal peridotites. Earth Planetary Science Letter **257**, 290–298.

Anders E. and Grevsse N. (1989) Abundances of the elements: Meteoritic and solar. Geochimica et Cosmochimica Acta **53**, 197–214.

Baker M. B. and Stolper E. M. (1994) Determining the composition of high–pressure mantle melts using diamond aggregates. Geochimica et Cosmochimica Acta **58**, 2811–2827.

Baker M. B. and Stolper E. M. (1994) Determining the composition of high-pressure mantle melts using diamond aggregates. Geochimica et Cosmochimica Acta **58**, 2811–2827.Bedini R. and Bodinier J. L. (1999) Distribution of incompatible trace elements between the constituents of spinel peridotite xenoliths: ICP–MS data from the East African Rift. Geochimica et Cosmochimica Acta **63**, 3883–3900.

Bodinier J. L., Vasseur G., Vernieres J., Dupuy C. and Fabries J. (1990) Mechanisms of Mantle Metasomatism: Geochemical Evidence from the Lherz Orogenic Peridotite. Journal of Petrology **31**, 597–628.

Brey G. and Kohler T. (1990) Geothermobarometry in four–phase lherzolites II. New thermobarometers, and practical assessment of existing thermobarometers. Journal of Petrology **31**, 1353–1378.

Brunelli D. and Seyler M. (2010) Asthenospheric percolation of alkaline melts beneath the St. Paul region (Central Atlantic Ocean). Earth Planetary Science Letter 289, 393–405.

Brunelli D., Paganelli E. and Seyler M. (2014) Percolation of enriched melts during incremental open–system melting in the spinel field: a REE approach to abyssal peridotites from the Southwest Indian Ridge. Geochimica et Cosmochimica Acta **127**, 190–203.

Brunelli D., Seyler M., Cipriani A., Ottolini L. and Bonatti E. (2006) Discontinuous melt extraction and weak refertilization of mantle peridotites at the Vema Lithospheric Section (Mid– Atlantic Ridge). Journal of Petrology **47**, 745–771.

Cherniak D. J. (2015) Nb and Ta diffusion in titanite. Chemical Geology **413**, 44–50.

Cherniak D. J. and Liang Y. (2007) Rare earth element diffusion in natural enstatite. Geochimica et Cosmochimica Acta **71**, 1324–1340.

D'Errico M. E., Warren J. M. and Godard M. (2016) Evidence for chemically heterogeneous Arctic mantle beneath the Gakkel Ridge. Geochimica et Cosmochimica Acta **174**, 291–312.

Dick H. J. B. and Bullen T. (1984) Chromian spinel as a petrogenetic indicator in abyssal and alpine–type peridotites and spatially associated lavas. Contributions to Mineralogy and Petrology **86**, 54–76.

Dygert N. and Liang Y. (2015) Temperatures and cooling rates recorded in REE in coex– isting pyroxenes in ophiolitic and abyssal peridotites. Earth Planetary Science Letter **420**, 151–161.

Dygert N., Kelemen P. B. and Liang, Y. (2017) Spatial variations in cooling rate in the mantle section of the Samail ophiolite in Oman: Implications for formation of lithosphere at mid–ocean ridges. Earth and Planetary Science Letters **465**, 134–144.

Ghiorso M. S., Hirschmann M. M., Reiners P. W. and Kress V. C. (2002) The pMELTS: a revision of MELTS for improved calculation of phase relations and major element partitioning related to partial melting of the mantle to 3 GPa. Geochemistry, Geophysics, Geosystems **3**, 1–35.

Harvey J., Yoshikawa M., Hammond S. J. and Burton K. W. (2012) Deciphering the trace element characteristics in Kil–bourne Hole peridotite xenoliths: melt–rock interaction andmetasomatism beneath the Rio Grande Rift, SW USA. Journal of Petrology **53**, 1709–1742.

Hellebrand E. and Snow J. E. (2003) Deep melting and sodic metasomatism underneath the highly oblique–spreading Lena Trough (Arctic Ocean). Earth and Planetary Science Letters **216**, 283–299.

Hellebrand E., Snow J. E., Dick H. J. B. and Hofmann A. W. (2001) Coupled major and trace elements as indicators of theextent of melting in mid–ocean–ridge peridotites. Nature **410**,677–681.

Hellebrand E., Snow J. E., Hoppe P. and Hofmann A. W. (2002) Garnet–field melting and late–stage refertilization in 'residual' abyssal peridotites from the Central Indian Ridge. Journal of Petrology **43**, 2305–2338.

Hellebrand E., Snow J. E., Mostefaoui S. and Hoppe P. (2005) Trace element distribution between orthopyroxene and clinopyroxene in peridotites from the Gakkel Ridge: a SIMS and NanoSIMS study. Contributions to Mineralogy and Petrology **150**, 486–504.

Iwamori H. (1994) ^{238}U–^{230}Th–^{226}Ra and ^{235}U–^{231}Pa disequilibria produced by mantle melting with porous and channel flows. Earth and Planetary Science Letters **125**, 1–16.

Johnson K. T. M. (1998) Experimental determination of partition coefficients for rare earth and high–field–strength elements between clinopyroxene, garnet, and basaltic melt at high pressures. Contributions to Mineralogy and Petrology **133**, 60–68.

Johnson K. T. M. and Dick H. J. B. (1992) Open system melting and temporal and spatial variation of peridotite and basalt at the Atlantis II Fracture Zone. Journal of Geophysical Research: Solid Earth 97, 9219–9241.

Johnson K. T. M., Dick H. J. B. and Shimizu N. (1990) Melting in the oceanic upper mantle: an ion microprobe study of diopsides in abyssal peridotites. Journal of Geophysical Research: Solid Earth **95**, 2661–2678.

Kelemen P. B., Hirth G., Shimizu N., Spiegelman M. and Dick H. J. B. (1997) A review of melt migration processes in the adiabatically upwelling mantle beneath oceanic spreading ridges. Philosophical Transactions: Mathematical, Physical and Engineering Science **355**, 283–318.

Kinzler R. J. and Grove T. L. (1992) Primary magmas of mid-ocean ridge basalts 1. Experiments and methods. Journal of Geophysical Research: Solid Earth **97**, 6885–6906.

Lee C. T. A., Harbert A. and Leeman W. P. (2007) Extension of lattice strain theory to mineral/mineral rare–earth element partitioning: An approach for assessing disequilibrium and developing internally consistent partition coefficients between olivine, orthopyroxene, clinopyroxene and basaltic melt. Geochimica et Cosmochimica Acta **71**, 481–496.

Liang Y. (2003) On the thermo–kinetic consequences of slab melting. Geophysical Research Letter **30**, 2270. http://dx.doi.org/ 10.1029/2003GL018969.

Liang Y. (2014) Time scales of diffusive re–equilibration in bi–mineralic systems with and without a fluid or melt phase. Geochimica et Cosmochimica Acta **132**, 274–287.

Liang Y. and Liu B. (2016) Simple models for disequilibrium fractional melting and batch melting with application to REE fractionation in abyssal peridotites. Geochimica et Cosmochimica Acta **173**, 181–197.

Liang Y. and Peng Q. (2010) Non–modal melting in an upwelling mantle column: steady–state models with applications to REE depletion in abyssal peridotites and the dynamics of melt migration in the mantle. Geochimica et Cosmochimica Acta **74**, 321– 339.

Liang Y., Sun C. and Yao L. (2013) A REE–in–two–pyroxene thermometer for mafic and ultramafic rocks. Geochimica et Cosmochimica Acta **102**, 246–260.

Liu B. and Liang Y. (2017) An introduction of Markov chain Monte Carlo method to geochemical inverse problems: Reading melting parameters from REE bundances in abyssal peridotites. Geochimica et Cosmochimica Acta **203**, 216–234.

Liu C.–Z., Snow J. E., Hellebrand E., Brugmann G., von der Handt A., Buchl A. and Hofmann A. W. (2008) Ancient, highly heterogeneous mantle beneath Gakkel ridge, Arctic Ocean. Nature **452**, 311–316.

Liu J., Carlson R. W., Rudnick R. L., Walker R. J., Gao S. and Wu F. (2012) Comparative Sr–Nd–Hf–Os–Pb isotope systematics of xenolithic peridotites from Yangyuan, North China Craton: additional evidence for a Paleoproterozoic age. Chemical Geology **332**, 1–14.

Lundstrom C. (2000) Models of U–series disequilibria generation in MORB: the effects of two scales of melt porosity. Physics of the Earth and Planetary Interiors **121**, 189–204.

McDonough W. F. and Sun S. S. (1995) The composition of the Earth. Chemical Geology **120**, 223–253.

Navon O. and Stolper E. (1987) Geochemical consequences of melt percolation: the upper mantle as a chromatographic column. The Journal of Geology **95**, 285–307.

Niu Y. and He´kinian R. (1997) Spreading–rate dependence of the extent of mantle melting beneath ocean ridges. Nature 385, 326– 329.

Quinn D. P., Saleeby J., Ducea M., Luffi P. and Asimow P. (2018) Late–Cretaceous con–struction of the mantle lithosphere beneath the central California coast revealed by Crystal Knob xenoliths. Geochemistry, Geophysics, Geosystems **19**, 3302–3346.

Salters V. J. M. and Dick H. J. B. (2002) Mineralogy of the mid– ocean–ridge basalt source from neodymium isotopic composition of abyssal peridotites. Nature **418**, 68–72.

Sambridge M. and Mosegaard K. (2002) Monte Carlo methods in geophysical inverse problems. Reviews of Geophysics **40**, 1009.

Sanfilippo A., Salters V., Tribuzio R. and Zanetti A. (2019) Role of ancient, ultra–depleted mantle in mid–ocean–ridge magmatism. Earth Planetary Science Letter **511**, 89–98.

Seyler M., Brunelli D., Toplis M. J. and Me´vel C. (2011) Multiscale chemical heterogeneities beneath the eastern Southwest Indian Ridge (52° E–68° E): Trace element compositions of along–axis dredged peridotites. Geochemistry, Geophysics, Geosystems 12, Q0AC15, doi:10.1029/2011GC003585.

Shimizu N. (1998) The geochemistry of olivine–hosted melt inclusions in a FAMOUS basalt ALV519–4–1. Physics of the Earth and Planetary Interiors **107**, 183–201.

Stosch H. G. (1982) Rare earth element partitioning between minerals from anhydrous spinel peridotite xenoliths. Geochimica et Cosmochimica Acta **46**, 793–811.

Stracke A., Genske F., Berndt J. and Koornneef J. M. (2019) Ubiquitous ultra–depleted domains in Earth's mantle. Nature Geoscience **12**, 851–855.

Stracke A., Snow J. E., Hellebrand E., von der Handt A., Bourdon B., Birbaum K. and Günther, D. (2011) Abyssal peridotite Hf isotopes identify extreme mantle depletion. Earth Planetary Science Letter **308**, 359–368.

Sun C. and Liang, Y. (2014) An assessment of subsolidus re–equilibration on REE distribution among mantle minerals olivine, orthopyroxene, clinopyroxene, and garnet in peridotites. Chemical Geology **372**, 80–91.

Van Orman J. A., Grove T. L. and Shimizu N. (2001) Rare earth element diffusion in diopside; influence of temperature, pressure, and ionic radius, and an elastic model for diffusion in silicates. Contributions to Mineralogy and Petrology **141**, 687–703.

Van Orman J. A., Grove T. L. and Shimizu N. (2002) Diffusive fractionation of trace elements during production and transport of melt in Earth's upper mantle. Earth Planetary Science Letter **198**, 93–112.

Voigt M. and von der Handt A. (2011) Influence of subsolidus processes on the chromium number in spinel in ultramafic rocks. Contributions to Mineralogy and Petrology **162**, 675–689.

Walter M. J. and Presnall D. C. (1994) Melting behavior of simplified lherzolite in the system $CaO–MgO–Al_2O_3–SiO_2–Na_2O$ from 7 to 35 kbar. Journal of Petrology **35**, 329–359.

Wang C., Liang Y. and Xu W. (2015) On the significance oftemperatures derived frommajor element and REE based two–pyroxene thermometers for mantle xenoliths from the North China Craton. Lithos **224–225**, 101–113.

Warren J. M. (2016) Global variations in abyssal peridotite compositions. Lithos **248–251**,193–219.

Warren J. M., Shimizu N., Sakaguchi C., Dick H. J. B. and Nakamura E. (2009) An assessment of upper mantle heterogeneity based on abyssal peridotite isotopic compositions. Journal of Geophysical Research 114, B122023, doi:10.1029/2008JB006186.

Witt–Eickschen G. and O'Neill H. S. C. (2005) The effect of temperature on the equilibrium distribution of trace elements between clinopyroxene, orthopyroxene, olivine and spinel in upper mantle peridotite. Chemical Geology **221**, 65–101.

Workman R. K. and Hart S. R. (2005) Major and trace element composition of the depleted MORB mantle (DMM). Earth Planetary Science Letter **231**, 53–72.

Yao L. (2015) Closure Temperature and Closure Pressure in Bi–Mineralic Systems with Applications to REE–in–Two–Mineral Thermobarometers. Brown University Ph.D. thesis.

Yao L. and Liang Y. (2015) Closure temperature in cooling bi–mineralic systems: I. Definition and with application to REE–in–two–pyroxene thermometer. Geochimica et Cosmochimica Acta **162**, 137–150.

Figure Captions

Fig. 1. (a) Forward simulation of REE patterns in residual solid, clinopyroxene (cpx), and orthopyroxene (opx) after 6% disequilibrium melting followed by subsolidus reequilibration. The solid lines represent REE patterns calculated using the multi-mineral disequilibrium melting model and melting parameters of $\varepsilon_{La}^{1300} = 0.01$ and $\mathbb{R} = 0.95$. The dashed lines represent the recalculated REE concentrations in the two pyroxenes at 1100ºC and 900ºC. (b) Comparison of REE patterns in residual solid, clinopyroxene, and orthopyroxene after 6% disequilibrium melting for two choices of opx grain size. The solid lines represent the case of $r_{cpx} = 1$ mm and the dashed lines are for $r_{opx} = 5$ mm. The grain size of cpx is assumed to be 1 mm. Parameters used in this simulation are as same as in (a). The temperature-dependent cpx-opx partition coefficients are from Sun and Liang (2014). Concentrations of REE are normalized to CI chondrite using the values of Anders and Grevesse (1989).

Fig. 2. Comparison of the temperatures derived from the REE-in-two-pyroxene thermometer of Liang et al. (2013, T_{REE}) and those calculated using the two-pyroxene thermometer of Brey and Kohler (1990, T_{BKN}) for the 9 mantle xenoliths and 12 abyssal peridotites included in this study (see text for a list of the source of data). All calculations were performed assuming a pressure of 1.5 GPa.

Fig. 3. Modal abundances of clinopyroxene (cpx), orthopyroxene (opx), and olivine (ol) in mantle xenoliths (a) and abyssal peridotites (b) selected in this study. The magenta lines in (a) are calculated using the melting reaction of Baker and Stolper (1994): 0.38 opx + 0.71 cpx + 0.13 spinel = 0.22 olivine +1 melt and for three choices of starting mantle mode. The light grey area in (b) is based on Warren (2016) for residual abyssal peridotites from around the world. The magenta curves in (b) represent melting paths based on pMELTS with potential temperature of 1330 ℃ and 150 ppm water content and three choices of starting mantle mode. Sample legends are the same as in Fig. 2.

Fig. 4. Comparison between observed (circles) and model derived (curves) REE+Y patterns in the bulk and two pyroxenes in the xenolith sample CK-2 (Quinn et al., 2018). Simulation results for three starting mantle modes are shown in panels (a), (b), and (c). The grey solid curves are MCMC predictions and the red solid curve represents the best-fit of the bulk REE+Y data. The solid blue and green curves represent the calculated REE abundances in cpx and opx, respectively, based on the inversed melting parameters of the best-fit of the bulk data. The dashed blue and green curves represent the model predicted subsolidus REE abundances in cpx and opx at $T = T_{REE}$, calculated using the temperature-dependent cpx-opx partition coefficients of Sun and Liang (2014). The sum of Pearson's Chi-square (χ^2_{sum}) is the sum of the Chi-squares of simulated bulk (red curve) and simulated cpx and opx after subsolidus re-equilibrium (dashed bulk and green curves). The open squares and black curve in (a) represent the cpx data and the best-fit result based on the cpx-alone melting model. For clarity, data from cpx-alone simulations were elevated by a factor of 5. Concentrations of REE are normalized to CI chondrite using the values of Anders and Grevesse (1989).

Fig. 5. Comparison between observed (circles) and model derived (curves) REE+Y patterns in the bulk and two pyroxenes in the abyssal peridotite sample Van7-85-49 (Warren et al., 2009). For a detailed explanation of symbols and curves, a reader is referred to the caption to Fig. 4.

Fig. 6. Variations of the apparent opx-cpx REE partition coefficient as a function of REE ionic radius for the xenolith sample CK-2 (a) and abyssal peridotite Van7-85-49 (b). The yellow circles represent the measured data. The magenta and black curves represent the model predicted apparent partition coefficients at the end of melting and at the subsoliduis temperature $T = T_{REE}$, respectively. The thin orange curves were calculated using a simple model for diffusive reequilibration between two minerals at the stated cooling rates (see text for details). The three dashed curves are the calculated opx-cpx REE partition coefficients using the model of Sun and Liang (2014).

Fig. 7. Comparison of the degree of melting derived from the cpx-alone inversion (F_{cpx}) and the degree of melting derived from inversion of the bulk sample (F_{bulk}) for the mantle xenoliths (a) and abyssal peridotites (b) selected in this study. The dashed lines and grey areas represent the 1:1 ratio within a ±2% range. The red dashed line in (a) connects the inversion results of sample YY-40B with primitive mantle (PM) and the depleted MORB mantle (DMM) starting compositions. Error bars are based on MCMC simulations. Sample legends are the same as in Fig. 2.

Fig. 8. Comparison of disequilibrium parameters (ε) and melt suction rate ($\mathbb{R}$) derived from the cpx-alone inversion and the bulk sample inversion for mantle xenoliths (a and c) and abyssal peridotites (b and d). Other details are the same as in Fig. 7.

Fig. 9. Variations of spinel Cr# (a) and bulk MgO content (b) as a function of the degree of melting for the mantle xenoliths and abyssal peridotites included in this study. The two dashed lines are based on the empirical expressions of Hellebrand et al. (2001) for fractional and batch melting. Symbols are the same as in Fig. 2.

Figure 1

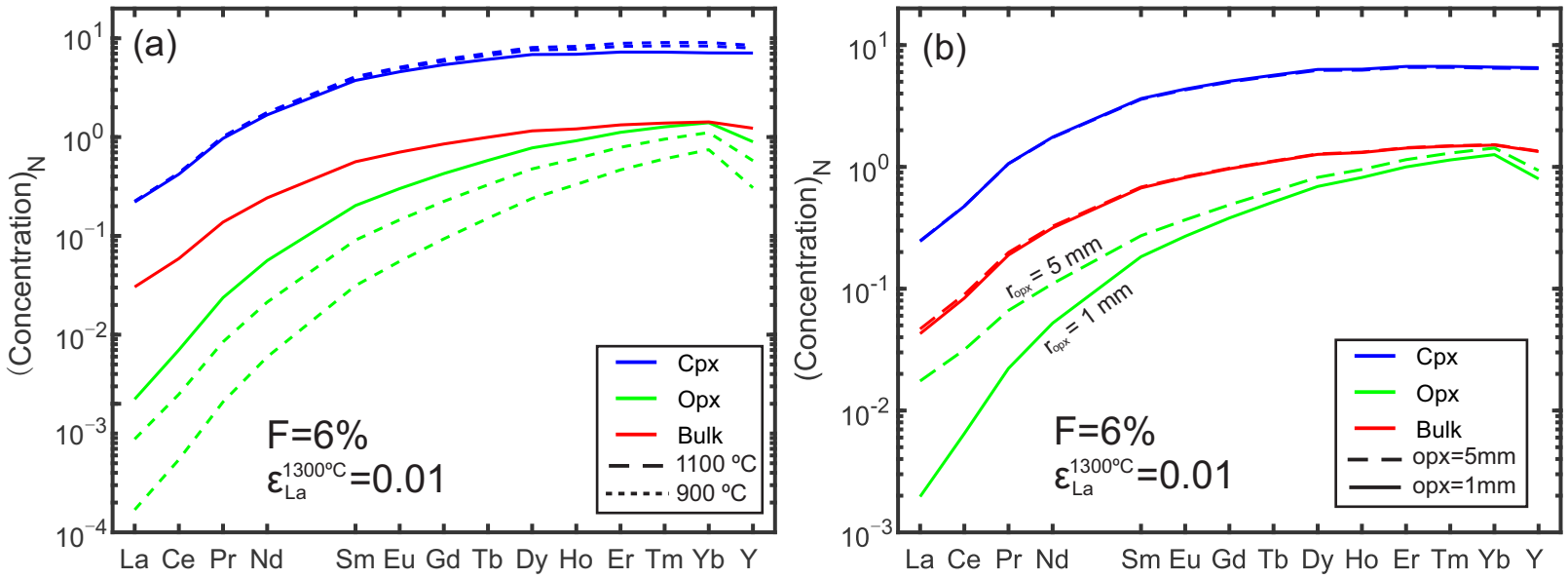

Fig. 1. (a) Forward simulation of REE patterns in residual solid, clinopyroxene (cpx), and orthopyroxene (opx) after 6% disequilibrium melting followed by subsolidus reequilibration. The solid lines represent REE patterns calculated using the multi-mineral disequilibrium melting model and melting parameters of $\varepsilon_{La}^{1300\,°C}$= 0.01 and $\mathbb{R}$ = 0.95. The dashed lines represent the recalculated REE concentrations in the two pyroxenes at 1100ºC and 900ºC. (b) Comparison of REE patterns in residual solid, clinopyroxene, and orthopyroxene after 6% disequilibrium melting for two choices of opx grain size. The solid lines represent the case of r_{cpx} = 1 mm and the dashed lines are for r_{opx} = 5 mm. The grain size of cpx is assumed to be 1 mm. Parameters used in this simulation are as same as in (a). The temperature -dependent cpx-opx partition coefficients are from Sun and Liang (2014). Concentrations of REE are normalized to CI chondrite using the values of Anders and Grevesse (1989).

Figure 2

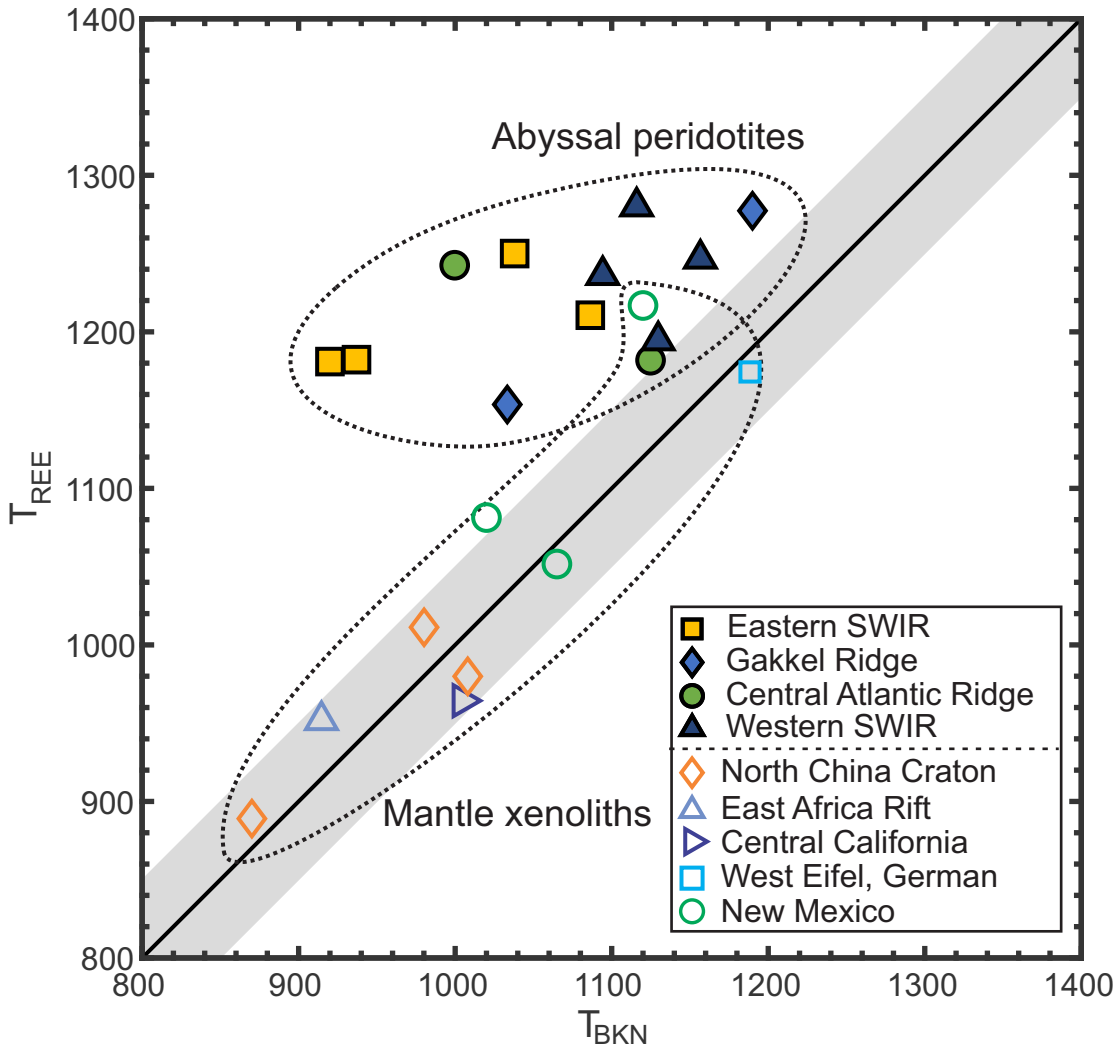

Fig. 2. Comparison of the temperatures derived from the REE-in-two-pyroxene thermometer of Liang et al. (2013, T_{REE}) and those calculated using the two-pyroxene thermometer of Brey and Kohler (1990, T_{BKN}) for the 9 mantle xenoliths and 12 abyssal peridotites included in this study (see text for a list of the source of data). All calculations were performed assuming a pressure of 1.5 GPa.

Figure 3

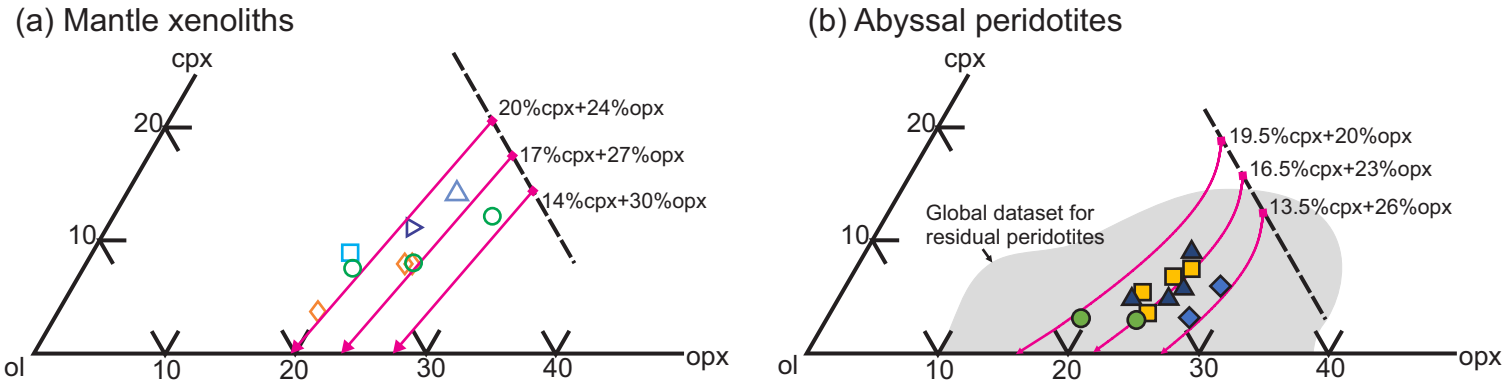

Fig. 3. Modal abundances of clinopyroxene (cpx), orthopyroxene (opx), and olivine (ol) in mantle xenoliths (a) and abyssal peridotites (b) selected in this study. The magenta lines in (a) are calculated using the melting reaction of Baker and Stolper (1994): 0.38 opx + 0.71 cpx + 0.13 spinel = 0.22 olivine + 1 melt and for three choices of starting mantle mode. The light grey area in (b) is based on Warren (2016) for residual abyssal peridotites from around the world. The magenta curves in (b) represent melting paths based on pMELTS with potential temperature of 1330 ℃ and 150 ppm water content and three choices of starting mantle mode. Sample legends are the same as in Fig. 2.

Figure 4

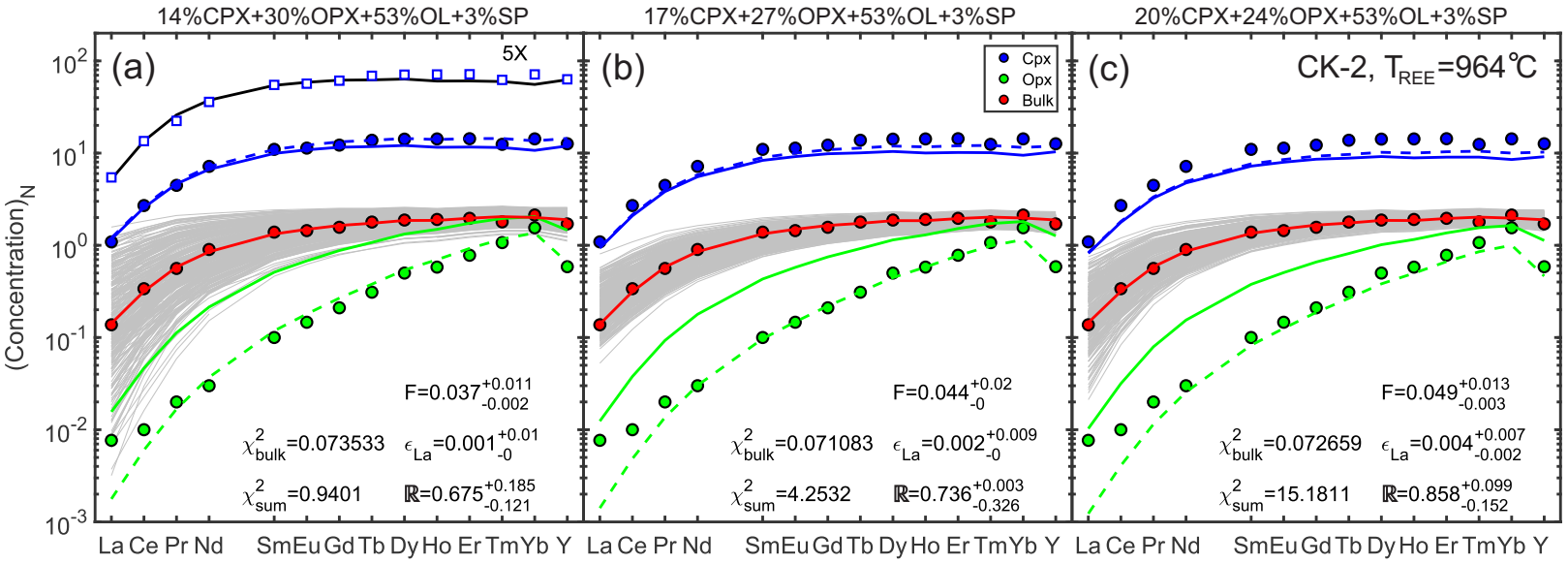

Fig. 4. Comparison between observed (circles) and model derived (curves) REE+Y patterns in the bulk and two pyroxenes in the xenolith sample CK-2 (Quinn et al., 2018). Simulation results for three starting mantle modes are shown in panels (a), (b), and (c). The grey solid curves are MCMC predictions and the red solid curve represents the best-fit of the bulk REE+Y data. The solid blue and green curves represent the calculated REE abundances in cpx and opx, respectively, based on the inversed melting parameters of the best-fit of the bulk data. The dashed blue and green curves represent the model predicted subsolidus REE abundances in cpx and opx at T = T_{REE}, calculated using the temperature-dependent cpx-opx partition coefficients of Sun and Liang (2014). The sum of Pearson's Chi-square (χ^2_{sum}) is the sum of the Chi-squares of simulated bulk (red curve) and simulated cpx and opx after subsolidus re-equilibrium (dashed bulk and green curves). The open squares and black curve in (a) represent the cpx data and the best-fit result based on the cpx-alone melting model. For clarity, data from cpx-alone simulations were elevated by a factor of 5. Concentrations of REE are normalized to CI chondrite using the values of Anders and Grevesse (1989).

Figure 5

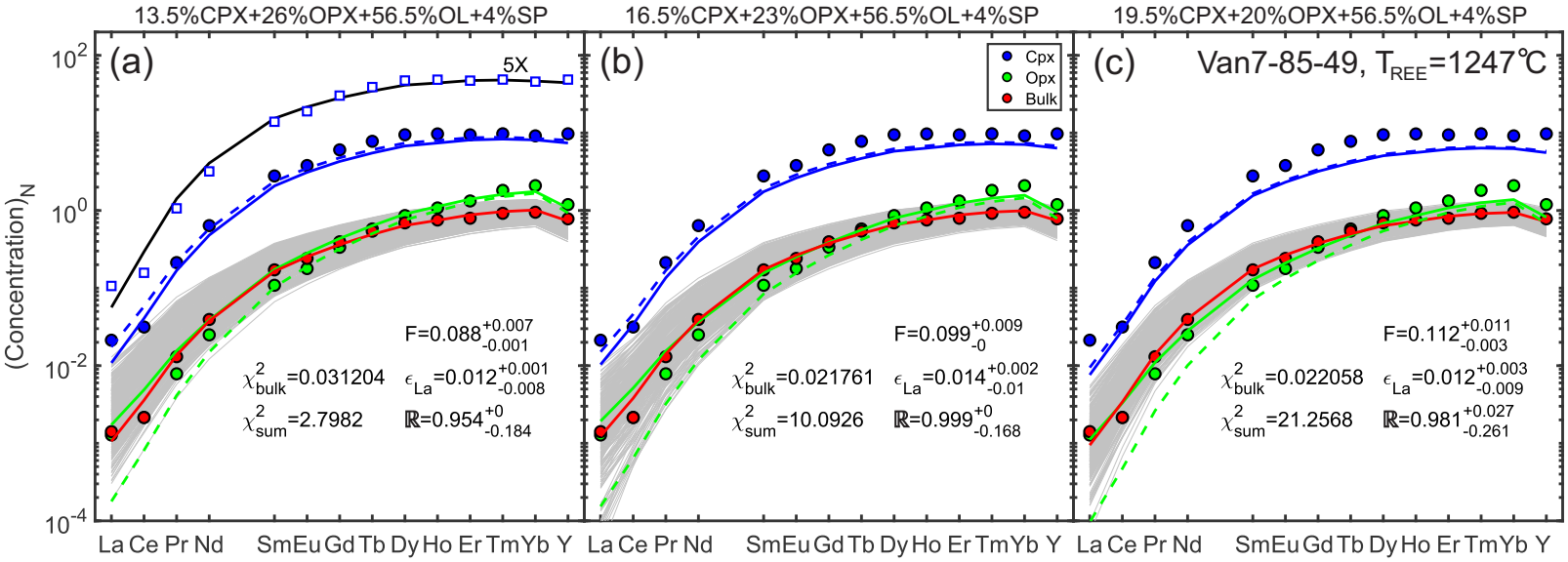

Fig. 5. Comparison between observed (circles) and model derived (curves) REE+Y patterns in the bulk and two pyroxenes in the abyssal peridotite sample Van7-85-49 (Warren et al., 2009). For a detailed explanation of symbols and curves, a reader is referred to the caption to Fig. 4.

Figure 6

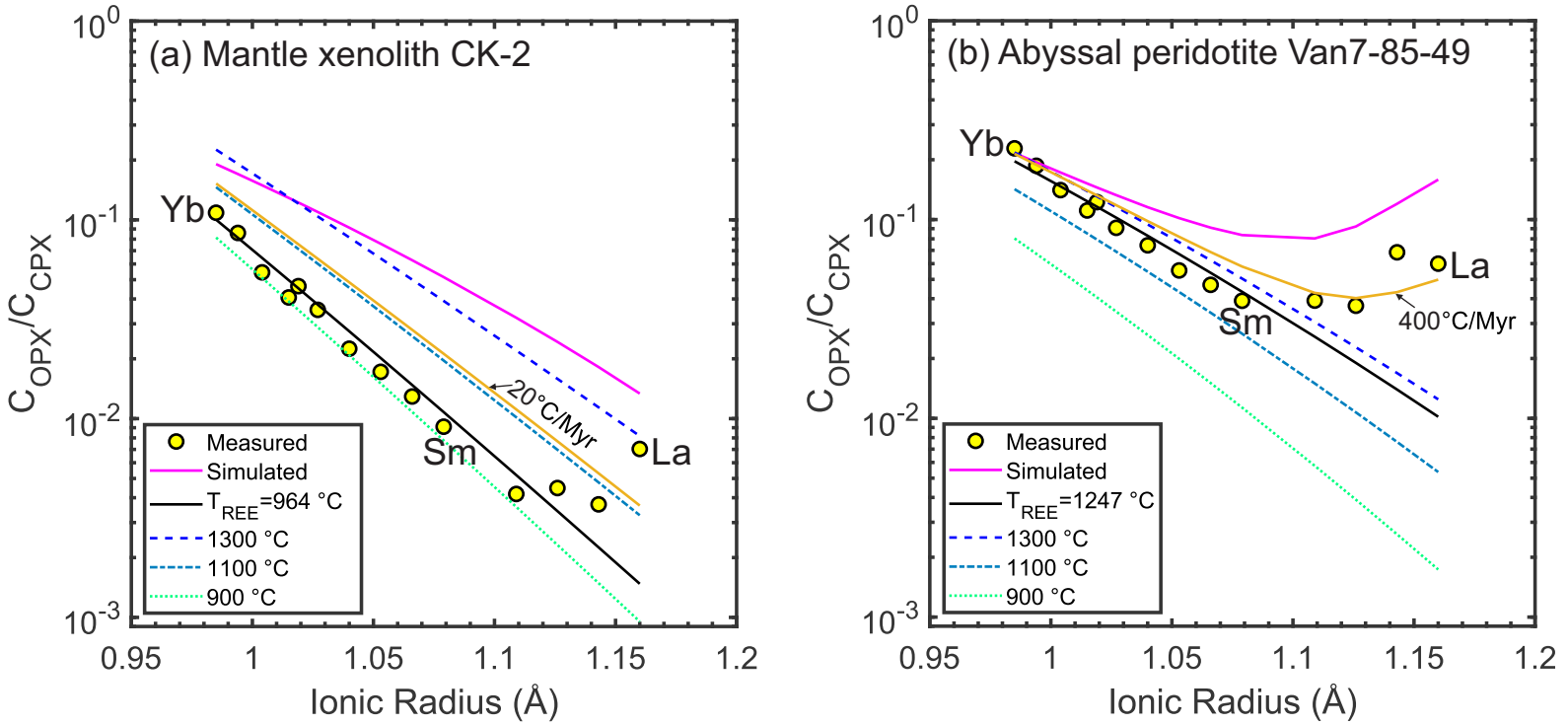

Fig. 6. Variations of the apparent opx-cpx REE partition coefficient as a function of REE ionic radius for the xenolith sample CK-2 (a) and abyssal peridotite Van7-85-49 (b). The yellow circles represent the measured data. The magenta and black curves represent the model predicted apparent partition coefficients at the end of melting and at the subsoliduis temperature T = T_{REE}, respectively. The thin orange curves were calculated using a simple model for diffusive reequilibration between two minerals at the stated cooling rates (see text for details). The three dashed curves are the calculated opx-cpx REE partition coefficients using the model of Sun and Liang (2014).

Figure 7

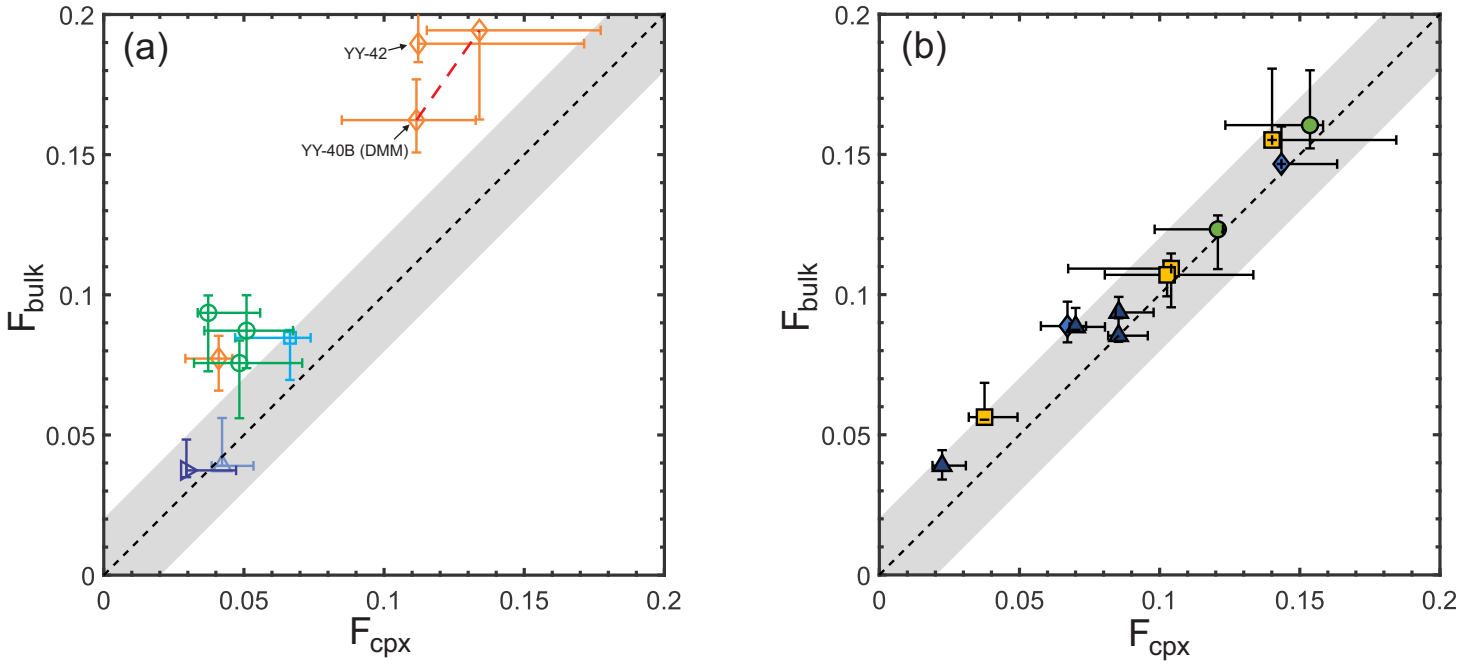

Fig. 7. Comparison of the degree of melting derived from the cpx-alone inversion (F_{cpx}) and the degree of melting derived from inversion of the bulk sample (F_{bulk}) for the mantle xenoliths (a) and abyssal peridotites (b) selected in this study. The dashed lines and grey areas represent the 1:1 ratio within a ±2% range. The red dashed line in (a) connects the inversion results of sample YY-40B with primitive mantle (PM) and the depleted MORB mantle (DMM) starting compositions. Error bars are based on MCMC simulations. Sample legends are the same as in Fig. 2.

Figure 8

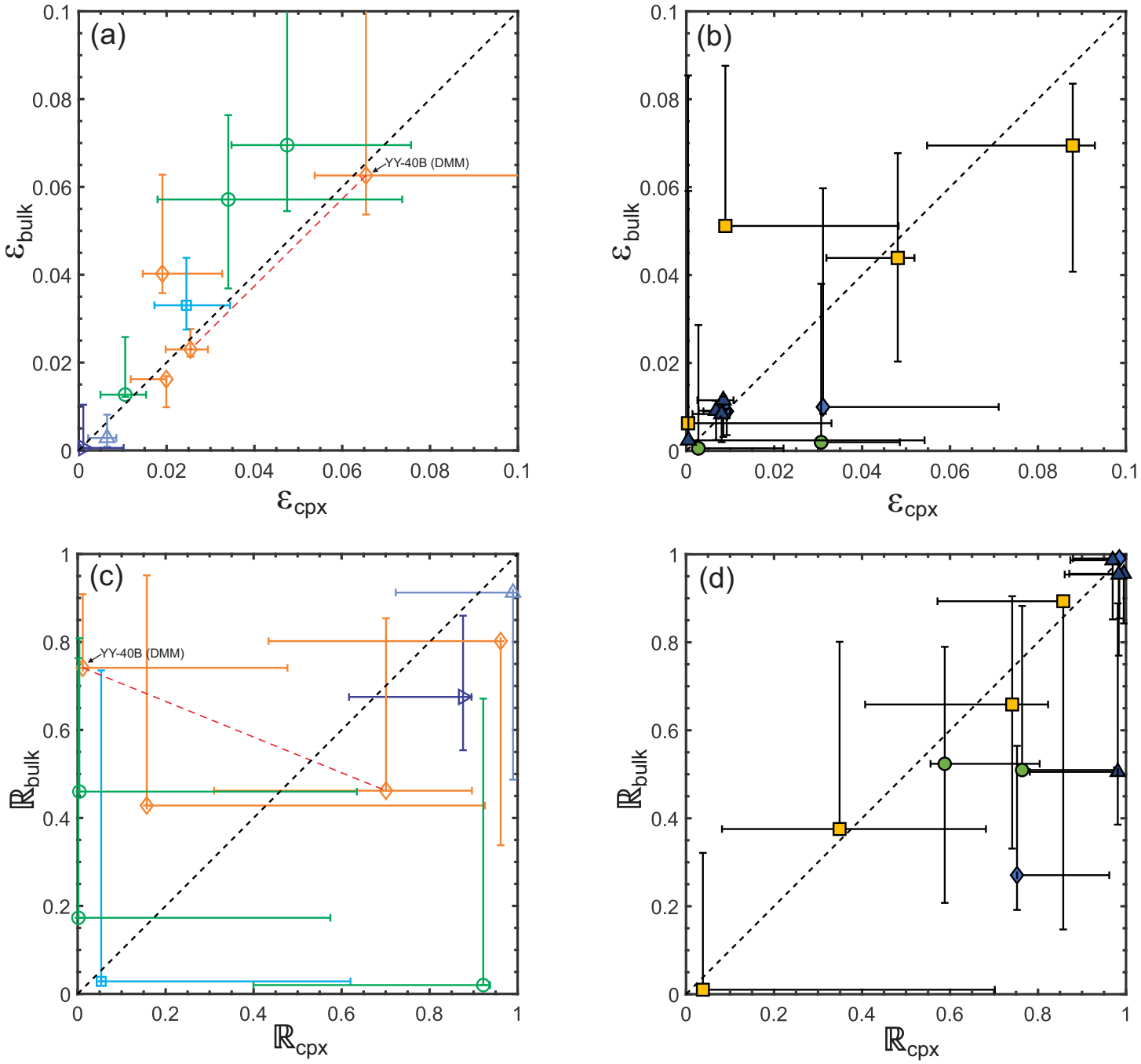

Fig. 8. Comparison of disequilibrium parameters (ε) and melt suction rate (ℝ) derived from the cpx-alone inversion and the bulk sample inversion for mantle xenoliths (a and c) and abyssal peridotites (b and d). Other details are the same as in Fig. 7.

Figure 9

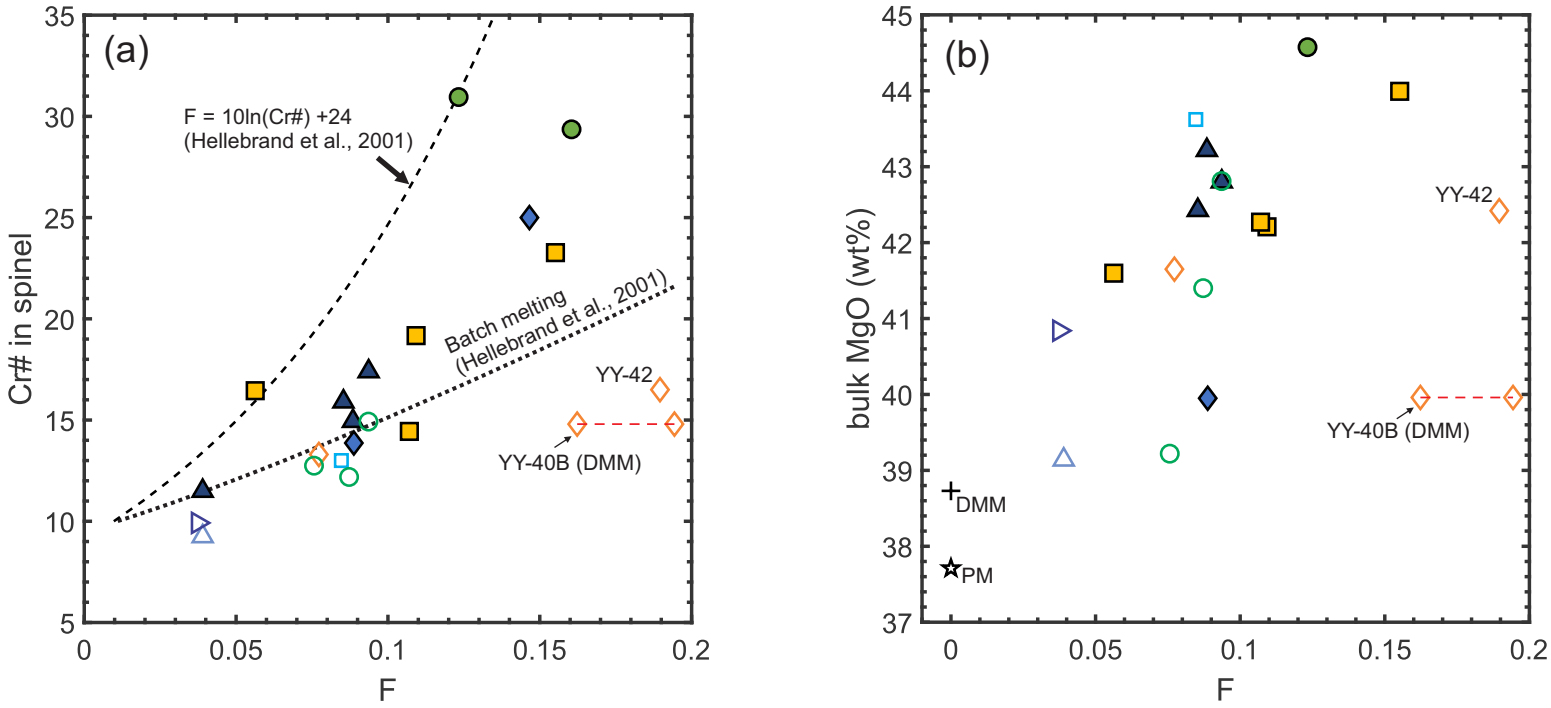

Fig. 9. Variations of spinel Cr# (a) and bulk MgO content (b) as a function of the degree of melting for the mantle xenoliths and abyssal peridotites included in this study. The two dashed lines are based on the empirical expressions of Hellebrand et al. (2001) for fractional and batch melting.